國　立　交　通　大　學
光　電　工　程　研　究　所

碩　士　論　文

氮化鎵二維光子晶體面射型雷射光學特性之研究

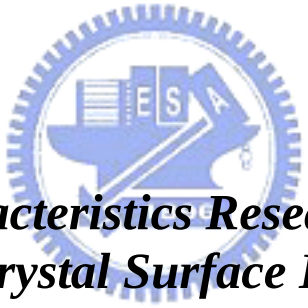

The Optical Characteristics Research of GaN-based 2D Photonic Crystal Surface Emitting Lasers

研究生：劉　子　維
指導教授：郭　浩　中　教授
盧　廷　昌　教授

中華民國九十七年六月

氮化鎵二維光子晶體面射型雷射光學特性之研究

The Optical Characteristics Research of GaN-Based 2D Photonic Crystal Surface Emitting Lasers

研 究 生：劉子維　　Student：Tzu-Wei Liu

指導教授：郭浩中　　Advisors：Hao-Chung Kuo

盧廷昌　　Tien-Chang Lu

國 立 交 通 大 學

光 電 工 程 研 究 所

碩 士 論 文

A Thesis

Submitted to Institute of Electro-Optical Engineering

College of Electrical Engineering and Computer Science

National Chiao Tung University

in partial Fulfillment of the Requirements

for the Degree of Master

in

Electro-Optical Engineering

June 2008

Hsinchu, Taiwan, Republic of China

中 華 民 國 九 十 七 年 六 月

氮化鎵二維光子晶體面射型雷射光學特性之研究

研究生：劉子維　　指導教授：郭浩中 教授　盧廷昌 教授

國立交通大學 光電工程研究所

摘 要

本篇論文研究探討氮化鎵二維光子晶體面射型雷射光學特性及回饋式理論。根據理論，在光子晶體周期結構中雷射出射必須滿足布拉格繞射條件。因此，考慮光致發光光譜中心波長 425 奈米，而設計光子晶體元件之晶格常數範圍 190 到 300 奈米。在室溫下，不同元件之雷射的波長範圍 395 到 425 奈米。以晶格常數 254 奈米為例，其線寬約 0.19 奈米，臨界激發光能量約 2.8mJ/cm^2。雷射的極化程度和發散角分別為 53%及<10 度。 其特性溫度大約 148K。 我們利用平面波展開法模擬 TE 能帶圖。從實驗數據研究光子晶體雷射之正規化頻率正好相對於(Γ1，K2，M3) 此三個能帶邊界，表示雷射發生只在特定能帶邊界上。從極化狀態可證實雷射模態確實存在(Γ1，K2，M3)此三個能帶邊緣。藉由二維耦合波模型可決定(Γ1，K2，M3)此三個能帶邊緣的耦合常數。Γ1 能帶邊緣有最大耦合常數相對於有最小臨界激發光能量。M3 帶邊緣有最小耦合常數相對於有最大臨界激發光能量。氮化鎵光子晶體雷射的優越的光學特性可應用在藍紫外光雷射等高輸出功率之光電元件。

The Optical Characteristics Research of GaN-based 2D Photonic Crystal Surface Emitting Lasers

Student : Tzu-Wei Liu **Advisor: Dr. H.C. Kuo**
Dr. T.C. Lu

Institute of electro-optical Engineering
National Chiao-Tung University

Abstract

In this thesis, we investigated the optical characteristics and distributed feedback theory of GaN-based 2D photonic crystal surface emitting lasers (PCSELs). According to the theory, the lasing behavior in the photonic crystal grating structure could only happen as the Bragg condition is satisfied. Therefore, the lattice constant is determined range from 190 to 300 nm considering PL peak centered at a wavelength of 425nm. The lasing wavelength is 395nm to 425nm for different device. We take the lattice constant 254nm for example, which with a linewidth of about 1.9 Å at room temperature. The pumping threshold energy density was estimated to be 2.8 mJ/cm^2. Moreover, the degree of polarization and divergent angle of the laser emission is about 53% and smaller than 10^o, respectively. The characteristic temperature is about 148K. We use plane wave expansion method (PWEM) to simulate the TE band diagram. All normalized frequency of investigated PC lasing wavelength can correspond to three band-edge frequencies (Γ1, K2, M3), which indicates the lasing action can only occur at specific band-edges. Polarization states confirm the existence of lasing modes at different band-edge (Γ1, K2, M3). The coupling coefficient at different band-edge (Γ1, K2, M3) can be obtained based on 2D couple wave model. The threshold gain at Γ1 is the lowest which corresponds to the highest coupling coefficient while the threshold gain at K3 is the highest which corresponds to the lowest coupling coefficient. Overall, the promising features of GaN-based PCSELs make it become the highly potential optoelectronic device in high power blue-violet emitter applications.

誌謝

碩士兩年飛逝，這兩年的學習指教鍛鍊且砥勵學生，讓學生培養碩士生應有獨立解決分析問題的能力，經過一番努力，總算能夠順利畢業。這是人生中重要的轉捩點，在期間由茫無頭緒到充滿興趣直到最後的成果出現，在在都要感謝實驗室這溫暖的大家庭，感謝兩位老師對我的論文不厭其煩的給予最完善且全面的建議，讓我在每次討論後亦能從另一觀點得到啟發，更彌補自身的不足，特別在此感謝兩位老師，記得當初郭老師對我選擇方向的時候，老師細心的解釋並且提供我建議，讓我感到很窩心。此外，不吝提攜後進的王老師，也在這兩年內，給我最精闢且獨到的見解，讓我更樂於在學問的殿堂中樂此不疲。除了實驗上老師給予我建議及方向，在做人處事上也從老師身上學習不少，感謝老師的建議以及鼓勵，讓我對於未來充滿自信。

直屬小強、宗鼎、立凡、士偉學長，指導我如何處理實驗上遇到的困難，也讓我學習到耐心謹慎求解才是科學的態度，因為美好的事物稍縱即逝，我想這句話用在做實驗上也是適用的吧。小朱學長我也常請教他理論和製程方面的事情，對於教導照顧學弟小朱學長真是不遺餘力，感謝他的指教。直屬學弟妹阿網小馬在實驗上也幫助我不少，相信在未來他們也會有自己的天空。碩二一起努力打拼的同學們也將各自往自己的目標前進，祝福你們。碩士求學期間，感謝很多學長們的幫忙，打球也會互揪，感覺到這是個溫馨的家庭，是很好的求學環境。

最後感謝家人和我的女朋友曉蓓，在我實驗忙碌的時候能給予我最大的支持，讓我能有信心順利的處理完事情，聽我抱怨實驗上的不順利，紓解我的壓力，有你們的鼓勵，是我進步的動力，謝謝你們無悔的付出，真的感謝有你們，真的。

2008/06　子維于

Contents

Figure Contents

Chapter 1

Introduction

1.1 Nitride-based materials

Nitride-based materials has been attracting much interest during past decades, because of their large direct wide band-gap characteristics and can be widely used in various optoelectronic devices such as flat panel displays, optical storage, automobiles, illumination and so on[1-4]. These kind III-V wide band-gap materials implies large band off-set characteristic which can be utilized in hetero-structure and provides better carrier confinement. These kind materials band-gap diagram cover the range from sub-eV to several few eV. This is a promising potential for construct full-color display and solid-state lighting, including light emitting diodes (LEDs) and laser diodes (LDs). Furthermore, larger band-gap results in higher bulk material dielectric strength (higher voltage per unit thickness) and strong excitonic energy, which leads to more compact and higher frequency device. In addition, the peak drift velocity of electron in GaN can be double that of Si and GaAs (10^7 cm/s) at much higher electric fields. Also, semiconductor with large band-gap can operate in higher temperature. These characteristics results in the high efficiency GaN-based electro-optic device. However, the problem currently being addressed in GaN and AlN materials on large defect densities, piezoelectric field effect and spontaneous polarization. It appears that growing defect-free GaN and AlN materials can be the limit to fabricate high quality and high power devices. Nowadays, there are many fundamental process breakthrough to tackle with how to control defects, threading dislocation, lattice mismatch in epitaxy. Therefore, the GaN-based materials with its superior properties make it a good candidate for the optoelectronic applications in next decades.

1.2Two dimensional photonic crystal lasers

In 1946, Edward Purcell first proposed that spontaneous from excited states of an atom can be significantly altered by placing it in a low loss cavity with dimensions on the order of the electromagnetic wavelength [5]. Recently, with the advent of semiconductor laser and the improvement of crystal growth and fabrication, there has been increasing interest in engineering of optical micro-cavity in semiconductor for light emission control. Photonic crystal is a dielectric structure arranged in periodic geometry. Like a crystalline solid in electronic band structure. So photonic crystal can exhibit one or more photonic band gaps (PBGs), with frequency in band gap unable to propagate in the crystal. Photonic crystal with photonic band gaps for photons have many advantages in controlling the light emission, wave propagate along specific direction and can be utilized in many optoelectronic devices. For instance, photonic crystal passive waveguide used as low loss channel for light propagation and resonator to keep the whole cavity with high Q characteristic, which can be a promising device in conjunction with Si based and III-V materials communication system. Semiconductor with these unique properties can not only be used as a versatile building block to construct photonic circuitry but also an active medium to control light emission [6]. Two kinds of semiconductor photonic lasers have been demonstrated. One is 2D photonic crystal nano-cavity lasers, and the other is 2D photonic crystal band-edge lasers.

I. 2D PC Nano-cavity lasers

In 1994, P. R. Berman *et al.* first presented that photonic crystal could be a reflective mirror around the cavity of a laser [7]. Then, in 1999 O. Painter practically demonstrated an optically pumped InGaAs-based 2-D PC nano-cavity laser emitting 1.55 micrometers [8]. The optical cavity he demonstrated consisted of a half-wavelength-thick waveguide for vertical confinement and a 2-D PC mirror for

lateral localization. A defect was introduced as a nano-cavity (a volume of 2.5 cubic half-wavelength, approximately 0.03 cubic micrometers) in the 2-D PC to trap photons inside. In 2004, Hong-Gyu Park *et al.* realized the electrically driven single-cell 2D-PC laser (λ=1519.7 nm) [9]. They used a sub-micrometer-sized semiconductor post placed at the center of the single-cell photonic crystal resonator to connect bottom electrode and achieved lasing action by current injection.

In 2005, nitride-based blue (about 488nm) photonic crystal membrane nano-cavity with Q factor about 800 was also reported by Y. S. Choi *et al.* [10]. They used photo-enhanced chemical etching to form a GaN membrane with a total thickness of 140 nm and patterned a photonic crystal cavity on it. Some resonance modes from the nano-cavities with lattice constant 180 nm could be observed in the photoluminescence (PL) emission.

II. 2D PC Band-edge lasers

According to the DFB theory, light at the photonic band-edge has zero group velocity and forms a standing wave due to 2D DFB effect. Specific band-edges induce not only in-plane coupling via DFB, but also diffraction normal to the PC plane, causing surface emission phenomena. In 1999, Noda *et al.* reported the electrically driven 2-D PC band-edge laser under pulsed operation [11]. The PC was a triangular-lattice structure composed of InP and air holes, which is integrated with an InGaAsP/InP multiple-quantum-well active layer by a wafer fusion technique. They demonstrated the single-mode, large-area and surface-emitting lasing action, and analyzed the lasing mechanism based on the satisfying of Bragg condition. Then, they further reported the room-temperature (RT) 2D PC band-edge laser under continuous wave (CW) operation in 2004 [12]. This opens a new road toward the large-area single-mode surface emitting laser.

1.3 Objectives of the thesis

Many works have been done mainly using organic, GaAs and InP material systems. However, few GaN-based PC lasers have been reported yet. In the point view of superior properties of GaN-based materials and PC specific characteristics, we came up with the idea that combined those advantages to generate novel form of next-generation lasers-photonic crystal surface emitting lasers (PCSELs). In this thesis, we report the study of the PCSELs, which consist in theory, design, fabrication and the characteristics of the lasers. We analyzed and discussed the properties of PCSELs, such as threshold, polarization states, spontaneous emission coefficient, characteristic temperature, divergence angle. We also exhibited new model to explain the feedback mechanism and the method to calculate coupling coefficient at different band-edge based on couple-wave theory. So, the GaN-based PCSELs device and its characteristics has been demonstrated and investigated.

1.4 Outline of the thesis

This essay has been organized in the following way. The first section of the paper will examine the history of nitride-based materials. Chapter 2 begins by laying out the theoretical dimensions of the research, the couple-wave theory and oscillation feedback mechanism. Chapter 3 describes the wafer preparation and fabrication of PCSELs. Chapter 4 describes the design, synthesis, characteristics and simulation of PCSELs. The last chapter assesses the conclusion and future work.

References

1. S. Nakamura, M. Senoh, N. Iwasa, and S. Nagahama, *Jpn. J. Appl.Phys.*, **34**, L797 (1995)
2. S. Nakamura, T. Mukai, and M. Senoh, *Appl. Phys. Lett.*,**64**, 1687 (1994)
3. S. Nakamura, M. Senoh, S.Nagahama, N.Iwasa, T. Yamada, T. Matsushita, Y. Sugimoto, and H.Kiyoku, *Appl. Phys. Lett.*, **70**, 868 (1997)
4. S. Nakamura, *Science*, **281**, 956 (1998)
5. E.M. Purcell *Phys. Rev.* 69, 681 (1946)
6. C. M. Lai, H. M. Wu, P. C. Huang, S. L. Peng, *Appl. Phys. Lett.*, **90**, 141106, (2007)
7. P. R. Berman, New York:Academic, (1994)
8. O. Painter, R. K. Lee, A. Scherer, A. Yariv, J. D. O`Brien, P. D. Dapkus, I. Kim, *Science*, **284**, 1819, (1999)
9. H. G. Park, S. H. Kim, S. H. Kwon, Y. G. Ju, J. K. Yang, J. H. Baek, S. B. Kim, Y. H. Lee, *Science*, **305**, 1444, (2005)
10. Y. S. Choi, K. Hennessy, R. Sharma, E. Haberer, Y. Gao, S. P. DenBaars, C. Meier, *Appl. Phys. Lett.*, **87**, 243101, (2005)
11. M. Imada, S. Node, A. Chutinan. and T. Tokuda, *Appl. Phys. Lett.*, **75**, 316, (1999)
12. D. Ohnishi, T. Okano, M. Imada, and S. Node, *Opt. Exp.,* **12**, 1562, (2004)

Chapter 2

Fundamentals of Photonic Crystal Surface Emitting Lasers

Introduction

A considerable amount of literature has been published on photonic crystal surface emitting lasers utilizing a 2D distributed feedback (DFB) mechanism [1-4]. The device features single longitudinal and transverse mode, lasing with large area and narrow beam divergence. To calculate photonic band-gap and the distribution of electric or magnetic field, there have been many theoretical analysis and methods developed, such as 2D plane wave expansion method [2,5] (PWEM), finite difference time domain [6,7] (FDTD), Transfer Matrix method and Multiple scattering method, etc. To optimize PCSELs structure, most experimental data agree with PWEM and FDTD. But there are some limitations while using these theoretical methods. 2D PWEM only applies to the infinite structure that is contradictory to actual device. FDTD method consumes numerous computer memories to simulate the real structure. Thus, we use the simple and convenient method couple-wave theory to describe the oscillation mechanism in PCSELs structure. Preliminary work on couple-wave theory was undertaken by Kogelnik and Shank [8], they presented the couple-wave analysis of distributed feedback lasers near the Bragg diffraction. As a result, we will focus on the fundamental of couple-wave theory.

2.1 Couple-wave theory [8,9]

Distributed feedback lasers do not utilize the conventional cavity mirrors, but provide feedback via backward Bragg scattering from periodic perturbations of the refractive index or the gain of the medium. Distributed feedback structures are compact and provide a high degree of spectral selection. In this section, we are focus more on the

electromagnetic aspects of light wave propagation, particularly for our photonic structures. We revolve around couple-wave theory to approximately solve the complex equations, which would be addressed numerically.

In order to use these approaches, we generally know at least that some of eigenmodes of a relatively simple waveguide configuration. The trick is to express the solution to some perturbed or more complex configuration in terms of these original basis set of eigenmodes. Then we can get general form of any dimension couple-wave equation.

To get started, we recall the fundamental wave equation to help us understand it. In a homogeneous, source-free and lossless medium, any time dependent harmonic electric field satisfy the vector wave equation

$$\nabla^2 \vec{E} + k_0{}^2 n^2 \vec{E} = 0 \tag{2.1}$$

where the time dependence of the electric field is assumed to be e^{jwt} , n is the refractive index and k_0 is the free space propagation constant.

And the electric field must satisfy the homogeneous wave equation such that:

$$\frac{\delta^2}{\delta z^2} E + k^2 E = 0 \tag{2.2}$$

Consider a multi-dielectric stack in which periodic corrugations are formed along one boundary as illustrated in Fig 2.1.

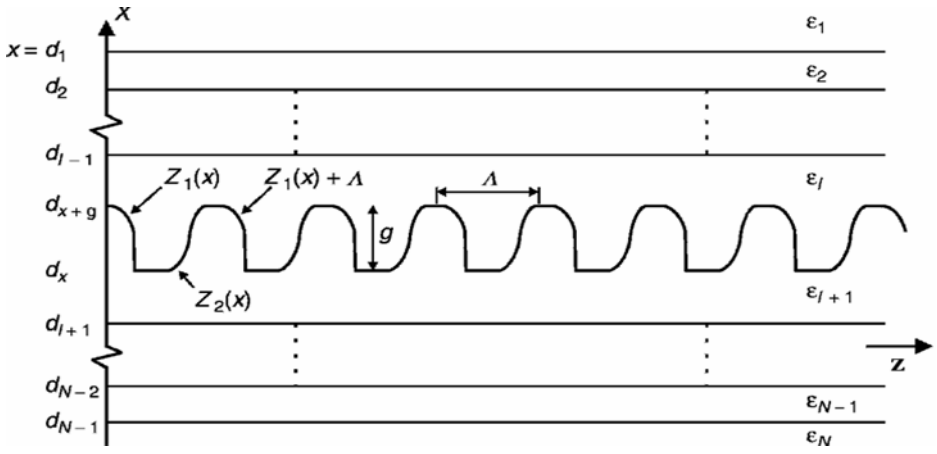

Figure 2.1 General multi-dielectric layers show the perturbation of refractive index and amplitude gain. $Z_1(x)$ and $Z_2(x)$ are two corrugated functions.

The material complex permittivity in each layer is denoted as ε_j while g and Λ are the height and the period of corrugation, respectively. With corrugations extending along the longitudinal direction, the wave propagation constant, k(z), could be written as

$$k^2(z) = w^2 \mu \varepsilon' \tag{2.3}$$

where w is the angular frequency and ε' is the complex permittivity. When the radiation frequency is sufficiently close to the resonance frequency, eqn (2.3) becomes

$$k^2 = k_0{}^2 n^2(z)\left(1 + j\frac{2\alpha(z)}{k_0 n(z)}\right) \tag{2.4}$$

where n(z) and $\alpha(z)$ are the refractive index and the amplitude gain coefficient, respectively. Within the grating region $dx \le x \le dx + g$, perturbation is considered so the refractive index and gain coefficient can be expressed in a Fourier form as

$$n(z) = n_0 + \Delta n \cos(2\beta_0 z + \Omega) \tag{2.5-1}$$

and

$$\alpha(z) = \alpha_0 + \Delta\alpha \cos(2\beta_0 z + \Omega + \theta) \tag{2.5-2}$$

Here, n_0 and α_0 are the steady-state values of the refractive index and amplitude gain, respectively. Δn and $\Delta\alpha$ are the amplitude perturbation terms, β_0 is the propagation constant and Ω is the non-zero residue phase at the z-axis origin. In the eqn (2.5-2), θ express the relative phase difference between perturbations of the refractive index and amplitude gain. Assume there is an incident plane wave entering the periodic, lossless waveguide at an angle of Φ as shown in Fig. 2.2. The propagation constant of the wave is assumed to be β_0.

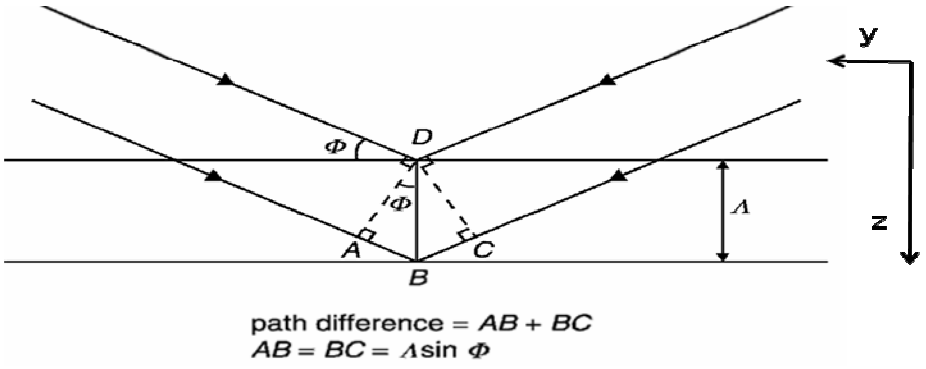

Figure 2.2 A simple model used to explain Bragg conditions in a periodic waveguide.

At each periodic interval of Λ, the incident wave will experience the same degree of refractive index change so that the incident wave will be reflected in the same direction. For a waveguide that consists of N periodic corrugations, there will be N reflected wavelets. In order that any two reflected wavelets add up in phase or interfere constructively, the phase difference between the reflected wavelets must be a multiple of 2π. In other words,

$$\beta_0(AB + BC) = \beta_0(2\Lambda \sin \Phi) = 2m\pi \tag{2.6}$$

where m is an integer. If the incident wave is now approaching more or less at a right angle to the wavefront (i.e. $\Phi \approx \pi/2$), eqn (2.6) becomes

$$2\beta_0\Lambda = 2m\pi \tag{2.7}$$

This is known as the Bragg condition and β_0 becomes the Bragg propagation constant. The integer m shown in the above equation defines the order of Bragg diffraction. Unless otherwise stated, first-order Bragg resonance (m =1) is assumed. Since a laser forms a resonant cavity, the Bragg condition must be satisfied [8]. Rearranging eqn (2.7) gives

$$\beta_0 \equiv \frac{2\pi n_0}{\lambda_B} \equiv \frac{n_0 w_B}{c} = \frac{\pi}{\Lambda} \tag{2.8}$$

where λ_B and w_B are the Bragg wavelength and the Bragg frequency, respectively. From eqn (2.8), it is clear that the Bragg propagation constant is related to the grating period. By altering the grating period, the Bragg wavelength can be shifted according to the specific application.

Using small signal analysis, the perturbations of the refractive index and gain are always smaller than their average values, i.e.

$$\Delta n << n_0, \quad \Delta\alpha << \alpha_0 \tag{2.9}$$

Substituting eqn (2.5) into (2.4) using the above assumption, generates

$$k^2(z) = k_0{}^2 n_0{}^2 + j2k_0 n_0 \alpha_0 + 2k_0[k_0 n_0 + j\alpha_0]\Delta n \cos(2\beta_0 z + \Omega)$$
$$+ 2jk_0 n_0 \Delta\alpha \cos(2\beta_0 z + \Omega + \theta) \quad (2.10)$$

With $k_0 n_0$ replaced by β and $\alpha_0 < \beta$, the above equation becomes

$$k^2(z) \approx \beta^2 + 2j\beta\alpha_0 + 2\beta[\frac{\pi\Delta n}{\lambda} + j\frac{\Delta\alpha}{2}e^{j\theta}]e^{j(2\beta 0 z+\Omega)}$$
$$+ 2\beta[\frac{\pi\Delta n}{\lambda} + j\frac{\Delta\alpha}{2}e^{-j\theta}]e^{-j(2\beta 0 z+\Omega)} \quad (2.11)$$

For the case when θ=0 , one can simplify (2.10) to[10]

$$k^2 \approx \beta^2 + 2j\beta\alpha_0 + 4\beta\left[\frac{\pi\Delta n}{\lambda} + j\frac{\Delta\alpha}{2}\right]\cos(2\beta_0 z + \Omega) \quad (2.12)$$

By controlling all the perturbed terms, one can define a parameter k [8,10] such that

$$k = \frac{\pi\Delta n}{\lambda} + j\frac{\Delta\alpha}{2} = k_i + jk_g \quad (2.13)$$

Here k_i includes all contributions from the refractive index perturbation whilst k_g covers all contributions from the gain perturbation. The parameter k introduced in the above equation is known as the coupling coefficient. After a series of simplifications, eqn (2.12) becomes

$$k^2 \approx \beta^2 + 2j\beta\alpha_0 + 4k\beta\cos(2\beta_0 z + \Omega) \quad (2.14)$$

On substituting the above equation back into the wave equation, one ends up with

$$\frac{d^2E}{dz^2} + \{\beta^2 + 2j\beta\alpha_0 + 2k\beta e^{j(2\beta 0 z+\Omega)} + 2k\beta e^{-j(2\beta 0 z+\Omega)}\}E = 0 \quad (2.15)$$

where the cosine function shown in eqn (2.14) has been expressed in phasor form. A trial solution of the scalar wave equation could be a linear superposition of two opposing traveling waves such that

$$E(z) = A(z)e^{-jkunz} + B(z)e^{jkunz} \quad (2.16)$$

with

$$k^2{}_{un} = \beta^2 + 2j\beta\alpha_0 \approx (\beta + j\alpha_0)^2 \quad (\because \alpha_0 << \beta) \quad (2.17)$$

In order to satisfy the Bragg condition shown earlier in eqn (2.8), the actual propagation constant, β, should be sufficiently close to the Bragg propagation

constant, β_0, to make the absolute difference between them much smaller than the Bragg propagation constant. In other words,

$$\left|\beta - \beta_0\right| << \beta_0 \tag{2.18}$$

Such a difference between the two propagation constants is commonly known as the detuning factor or detuning coefficient, δ, which is defined as

$$\delta = \beta - \beta_0 \tag{2.19}$$

The trial solution can be expressed in terms of the Bragg propagation constant, i.e.

$$E(z) = C(z)e^{-\alpha z}e^{-j\beta 0 z} + D(z)e^{\alpha z}e^{j\beta 0 z} = R(z)e^{-j\beta 0 z} + S(z)e^{j\beta 0 z} \tag{2.20}$$

where R(z) and S(z) are complex amplitude terms. Since the grating period Λ in a DFB semiconductor laser is usually fixed and so is the Bragg propagation constant, it is more convenient to consider eqn (2.20) as the trial solution of the scalar wave equation. By substituting eqn (2.20) into eqn (2.15), one ends up with the following equation

$$\begin{aligned}&(R''-2j\beta_0 R'-\beta_0^2 R+\beta^2 R+2j\beta\alpha_0 R)e^{-j\beta 0 z}\\&+(S''+2j\beta_0 S'-\beta_0^2 S+\beta^2 S+2j\beta\alpha_0 S)e^{j\beta 0 z}\\&+2k\beta(e^{2j\beta 0 z}e^{j\Omega}+e^{-2j\beta 0 z}e^{-j\Omega})\cdot(\mathrm{Re}^{-j\beta 0 z}+Se^{j\beta 0 z})=0\end{aligned} \tag{2.21}$$

where R' and R'' are the first- and second-order derivatives of R. Similarly, S' and S'' represent the first- and second-order derivatives of S. With a 'slow' amplitude approximation, high-order derivatives like R'' and S'' become negligible when compared with their first-order terms. By separating the above equation into two groups, each having similar exponential dependence, one can get the following pair of coupled wave equations

$$-\frac{dR}{dz}+(\alpha_0 - j\delta)R = jkSe^{-j\Omega} \tag{2.22}$$

$$\frac{dS}{dz}+(\alpha_0 - j\delta)S = jk\,\mathrm{Re}^{j\Omega} \tag{2.23}$$

Equation (2.22) collects all the exp(- $j\beta_0 z$) phase terms propagating along the positive z direction, whilst eqn (2.23) gathers all the exp($j\beta_0 z$) phase terms propagating along the negative direction. Since $|\delta| << \beta$, other rapidly changing phase terms such as exp($\pm j3\beta_0 z$) have been dropped. In deriving the above equations, the following approximation has been assumed

$$\frac{\beta^2 - \beta_0^2}{2\beta_0} \approx \beta - \beta_0 = \delta \tag{2.24}$$

Following the above procedures, one ends up with a similar pair of coupled wave equations for a non-zero relative phase difference between the refractive index and the gain perturbation (i.e. $\theta \neq 0$) such that

$$-\frac{dR}{dz} + (\alpha_0 - j\delta)R = jk_{RS}\,\mathrm{Re}^{-j\Omega} \tag{2.25}$$

$$\frac{dS}{dz} + (\alpha_0 - j\delta)S = jk_{SR}\,\mathrm{Re}^{j\Omega} \tag{2.26}$$

where

$$k_{RS} = k_i + jk_g e^{-j\theta} \tag{2.27}$$

is the general form known as the forward coupling coefficient and

$$k_{SR} = k_i + jk_g e^{j\theta} \tag{2.28}$$

is the backward coupling coefficient.

It is contrary to Fabry Perot lasers, where optical feedback is come from the laser facets. Optical feedback in DFB lasers is originated from along the active layer where corrugations are fabricated. From the above scalar equation, the couple-wave equation can be established in the general form, which is for one dimensional situation. Following we will discuss two dimensional optical coupling based on above couple-wave theory. For our GaN-based photonic structure, we assume that since the carriers in the InGaN layers are confined in the wall, they do posses a significant in-plane dipole, which can couple to TE mode. Therefore, we centered on TE like mode in

square lattice for 2D case.

2.2 2D couple-wave model

Preliminary numerical works have been done by Sakai, Miyai, and Noda [12,13]. Here, we cite their papers as references to help us understand the 2D couple-wave model.

The 2D PC structure investigated here consists of an infinite square lattice with circular air holes in the x and y directions, as shown in Fig 2.3. The structure is assumed to be uniform in the z direction. We don't consider the gain effects during calculation. We do calculate the resonant mode frequency as a function of coupling coefficient. The scalar wave equation for the magnetic field Hz in the TE mode can be written as [14]

$$\frac{\partial^2 Hz}{\partial x^2}+\frac{\partial^2 Hz}{\partial y^2}+k^2 Hz=0 \tag{2.30}$$

where [15]

$$k^2=\beta^2+2j\alpha\beta+2\beta\sum_{G\neq 0}k(G)\exp\left[j(G\cdot r)\right] \tag{2.31}$$

G=($m\beta_0$, $n\beta_0$) is the reciprocal lattice vector, m and n are arbitrary integers, $\beta_0=2\pi/a$ where a is the lattice constant, $\beta=n_{av}w/c$ where n_{av} is the averaged refractive index, $k(G)=\pi n_G/\lambda$ is the coupling constant, where n_G is the Fourier coefficient of the periodic refractive-index modulation and λ is the Bragg wavelength given by $\lambda=an_{av}$. In the eqn (2.31), we set $\alpha,\alpha_G << \beta_0, n_G << n_0$. We do consider Γ point, in which when it is satisfy the second order Bragg diffraction , it will induce 2D optical coupling and result in surface emission. The coupling constant $\kappa(G)$ can be expressed as

$$\kappa(G)=\frac{\pi}{\lambda}n(G)+j\frac{1}{2}\alpha(G) \tag{2.32}$$

where $n(G)$ is the Fourier coefficient of periodic refractive index modulation and λ is the Bragg wavelength given by $\lambda=an_{av}$.

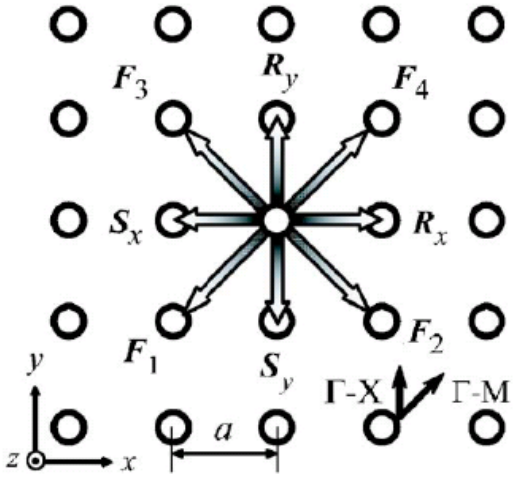

Figure 2.3 Schematic diagram of eight propagation waves in square lattice PC structure

In eqn (2.31), the periodic variation in the refractive index is included the small perturbation in third term through the Fourier expansion. In the Fourier expansion, the periodic perturbation terms generates an infinite set of diffraction orders. However, as the cavity mode frequency is sufficient close to the Bragg frequency, only the second order diffraction and below can do significant contribution, others can consider to be neglected. Therefore, we focus on diffraction order with $|m|+|n| \le 2$ to discuss. The corresponding coupling coefficient constant κj (j=1, 2, 3) are denoted as

$$\kappa_1 = \kappa(G)\|G| = \beta_0$$

$$\kappa_2 = \kappa(G)\|G| = \sqrt{2}\beta_0 \qquad (2.33)$$

$$\kappa_3 = \kappa(G)\|G| = 2\beta_0$$

while considering infinite structure, the magnetic field can be described by the Bloch mode [14],

$$Hz(r) = \sum_G h_G \exp[j(k+G)\cdot r] \qquad (2.34)$$

h_G is the amplitude of each plane wave, k is the wave vector in the first Brillouin zone and when it is the Γ point, it comes to zero. However, in the case of finite structure, h_G is not a constant but a function of vector space. For 2D case, there are eight

propagating waves in PC structure denoted as Rx, Sx, Ry, Sy, F_1, F_2, F_3, F_4 showed in Fig 2.3, those are the amplitudes of four propagating waves in the x, -x, y, -y directions and four propagating waves in Γ-M direction, respectively. Those correspond to h_G in eqn (2.34). Here, we do consider these basic wave vectors along the Γ-X directions with $|\kappa + G| = \beta_0$ and Γ-M directions with $|\kappa + G| = \sqrt{2}\beta_0$. The contribution of the higher order waves with $|\kappa + G| \geq 2\beta_0$, are considered to be negligible. We should note that the basic waves and higher order waves are partial waves of the Bloch mode, so they have the same eigenvalue β for specific resonant cavity mode.

The magnetic field in this case can be rewritten as

$$Hz = Rx(x,y)e^{-j\beta 0x} + Sx(x,y)e^{j\beta 0x} + Ry(x,y)e^{-j\beta 0y} + Sy(x,y)e^{j\beta 0y} + F_1 e^{j\beta 0x + j\beta 0y} + F_2 e^{-j\beta 0x + j\beta 0y} + F_3 e^{j\beta 0x - j\beta 0y} + F_4 e^{-j\beta 0x - j\beta 0y} \quad (2.35)$$

Put eqn (2.35) and eqn (2.31) into the wave eqn (2.30), and comparing the equal exponential terms, we obtain eight wave equations

$$(\beta - \beta_0)Rx + \kappa_3 Sx - \kappa_1(F_2 + F_4) = 0 \quad (2.36a)$$

$$(\beta - \beta_0)Sx + \kappa_3 Rx - \kappa_1(F_1 + F_3) = 0 \quad (2.36b)$$

$$(\beta - \beta_0)Ry + \kappa_3 Sy - \kappa_1(F_3 + F_4) = 0 \quad (2.36c)$$

$$(\beta - \beta_0)Sy + \kappa_3 Ry - \kappa_1(F_1 + F_2) = 0 \quad (2.36d)$$

$$(\beta - 2\beta_0)\frac{F_1}{2} - \kappa_1(Sx + Sy) = 0 \quad (2.36e)$$

$$(\beta - 2\beta_0)\frac{F_2}{2} - \kappa_1(Rx + Sy) = 0 \quad (2.36f)$$

$$(\beta - 2\beta_0)\frac{F_3}{2} - \kappa_1(Sx + Ry) = 0 \quad (2.36g)$$

$$(\beta - 2\beta_0)\frac{F_4}{2} - \kappa_1(Rx + Ry) = 0 \quad (2.36h)$$

In the above equations, we assume $\beta / \beta_0 \approx 1$, since we take optical coupling at Γ point as an example.

These derivations illustrate the coupling among the propagating waves in square lattice PC structure. We take eqn (2.36) for example. It describes the net wave superposition along the x-axis, including the coupling of two waves propagating at opposite directions, Rx and Sx, with a coupling coefficient κ_3. And the coupling of higher order waves F_2 and F_4, with a coupling coefficient κ_1. The coupling κ_3 provides the main distributed feedback. From above derivations, we know that the orthogonal couplings occur via intermediate coupling of the basic and higher order waves. One thing we should noted that the coupling coefficient κ_2 does not exist in eqn (2.36). In the numerical view which describes the basic waves directly couple to orthogonal directions. This physically can be explained in this way: ways of TE modes have their electric field parallel to the PC plane, so that the electric field directions of the two waves propagating in the perpendicular directions are orthogonal to one another, hence the overlap integral of the two waves vanishes.

By using 2D plane wave expansion method, the band dispersion curves for TE like modes in Fig 2.4 can be obtained. The condition is limited at the vicinity near Bragg frequency.

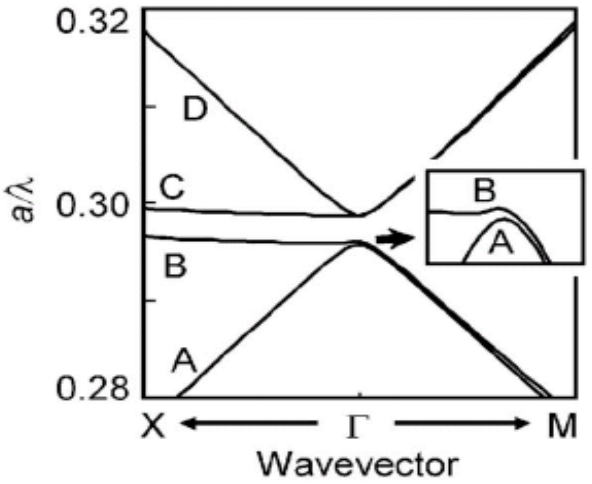

Figure 2.4 Dispersion relationship for TE like modes, calculated using the 2D PWEM

By solving eqn (2.36) . The cavity mode frequency can be obtained. There are three

cavity mode frequencies denoted as $w_A\ w_B\ w_C\ w_D$, with one degenerated.

$$w_A = \frac{c}{n_{av}}(\beta_0 - \kappa_3)(1 - \frac{8\kappa_1^2}{\beta_0^2 - \kappa_3^2})$$

$$w_B = \frac{c}{n_{av}}(\beta_0 - \kappa_3)$$

$$w_{C,D} = \frac{c}{n_{av}}(\beta_0 + \kappa_3)(1 - \frac{4\kappa_1^2}{\beta_0^2 - \kappa_3^2}) \qquad (2.37)$$

The frequencies w_A and w_B at the lower band-edges are non-degenerated, while two of the frequencies w_c and w_D at higher band-edge are degenerated. In the physical meaning, the resonant mode symmetries are different. The resonant mode at band-edge C and D are symmetric, which allows this mode to couple to external field more easily. The characteristics of these resonant modes are essentially leaky [16]. The resonant mode at band-edge A and B are anti-symmetric, resulting in less coupling to the external field. Therefore, the quality factor for band-edge A and B are higher than C and D. It is expected that the lasing behavior is occurred at either A or B. However, band B is flat around Γ point in the Γ-X direction. Light at band-edge B can couple to leaky mode with a wave vector slightly shifted from Γ point, resulting in coupling to the external field. Thus, band-edge B becomes leaky.

So far we have understood the fundamental couple-wave theory and how to calculate their cavity mode frequency. For our GaN-based PCSELs, we design the triangular lattice with TE-like mode to tell the differences between square lattice structure. Therefore, in next section, we develop a new model to explain the DFB feedback mechanism based on couple-wave theory. According to our measurement, we found that the lasing action occurred at Γ1, K2, M3 point band-edges. We tried to solve the wave equations at these band-edges and derive the coupling coefficients. All of detail will be described numerically in next section.

2.3 Couple-wave model for triangular lattice PCSELs

Light at the photonic band-edge has zero group velocity and forms a standing wave due to 2D DFB effect. Laser oscillation is expected to occur at any band-edge, if the gain threshold is achieved. Therefore, we focus on the coupling waves at Γ1, K2, M3 band-edges according to our lasing behaviors.

I. Γ1 numerical results

The 2D PC structure investigated here consists of an infinite triangular lattice with circular air holes in the x and y directions, as shown in Fig 2.5. The structure is assumed to be uniform in the z direction. We don't consider the gain effects during calculation. While considering infinite structure, the magnetic field can be described by the Bloch mode [14],

$$Hz(r) = \sum_{G} h_G \exp[j(k+G)\cdot r] \tag{2.34}$$

where

$$\begin{aligned} Hz = {} & H_1(x,y)e^{-i\beta 0\hat{x}} + H_2 e^{-i\beta 0(\frac{1}{2}\hat{x}+\frac{\sqrt{3}}{2}\hat{y})} + H_3 e^{-i\beta 0(\frac{-1}{2}\hat{x}+\frac{\sqrt{3}}{2}\hat{y})} \\ & + H_4 e^{i\beta 0\hat{x}} + H_5 e^{-i\beta 0(\frac{-1}{2}\hat{x}-\frac{\sqrt{3}}{2}\hat{y})} + H_6 e^{-i\beta 0(\frac{1}{2}\hat{x}-\frac{\sqrt{3}}{2}\hat{y})} \end{aligned} \tag{2.38}$$

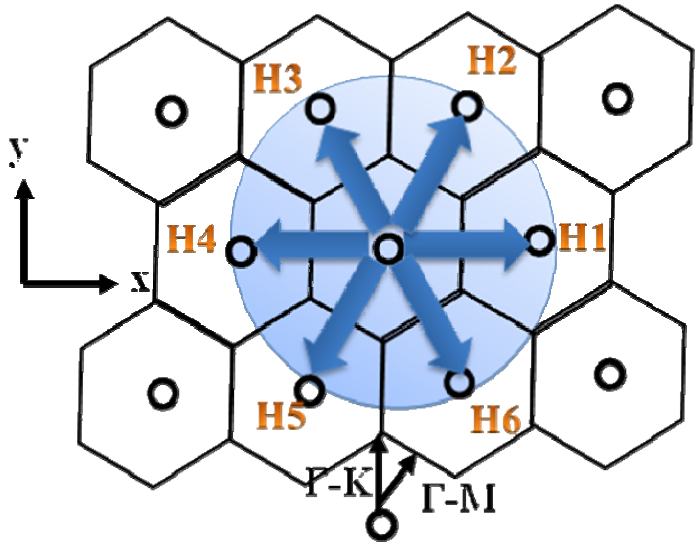

Figure 2.5 Schematic diagram of six propagation waves in triangular lattice for Γ1 point

put eqn (2.38) and eqn (2.31) into the wave eqn (2.30), and comparing the equal

exponential terms, we obtain six wave equations

$$-\frac{\partial}{\partial x}H_1+(-\alpha-i\delta)H_1=-i\frac{\kappa_1}{2}(H_2+H_6)+i\frac{\kappa_2}{2}(H_3+H_5)+i\kappa_3 H_4 \quad (2.39a)$$

$$-\frac{1}{2}\frac{\partial}{\partial x}H_2-\frac{\sqrt{3}}{2}\frac{\partial}{\partial y}H_2+(-\alpha-i\delta)H_2=-i\frac{\kappa_1}{2}(H_1+H_3)+i\frac{\kappa_2}{2}(H_4+H_6)+i\kappa_3 H_5 \quad (2.39b)$$

$$-\frac{1}{2}\frac{\partial}{\partial x}H_3-\frac{\sqrt{3}}{2}\frac{\partial}{\partial y}H_3+(-\alpha-i\delta)H_3=-i\frac{\kappa_1}{2}(H_2+H_4)+i\frac{\kappa_2}{2}(H_1+H_5)+i\kappa_3 H_6 \quad (2.39c)$$

$$\frac{\partial}{\partial x}H_4+(-\alpha-i\delta)H_4=-i\frac{\kappa_1}{2}(H_3+H_5)+i\frac{\kappa_2}{2}(H_2+H_6)+i\kappa_3 H_1 \quad (2.39d)$$

$$\frac{1}{2}\frac{\partial}{\partial x}H_5+\frac{\sqrt{3}}{2}\frac{\partial}{\partial y}H_5+(-\alpha-i\delta)H_5=-i\frac{\kappa_1}{2}(H_4+H_6)+i\frac{\kappa_2}{2}(H_1+H_3)+i\kappa_3 H_2 \quad (2.39e)$$

$$-\frac{1}{2}\frac{\partial}{\partial x}H_6+\frac{\sqrt{3}}{2}\frac{\partial}{\partial y}H_6+(-\alpha-i\delta)H_6=-i\frac{\kappa_1}{2}(H_1+H_5)+i\frac{\kappa_2}{2}(H_2+H_4)+i\kappa_3 H_3 \quad (2.39e)$$

where, H_1, H_2, H_3, H_4, H_5, and H_6 express the envelope magnetic field distributions of individual light waves propagating in the six equivalent Γ-M directions: 0°, +60°, +120°,+180°, +240°, and +300° with respect to the x-axis. κ_1, κ_2, and κ_3 are the coupling coefficients between light waves propagating at 60° to each other (H_1 and H_2, H_2 and H_3,and so on), at 120° (H_1 and H_3, H_2 and H_4, and so on), and at 180° (H_1 and H_4, H_2 and H_5, and so on), respectively. δ is the deviation of the wave number β (expressed as $2\pi\nu$/c, where ν is the frequency and c is the velocity of light) from the fundamental propagation constant β_0 (equal to $4\pi/\sqrt{3}a$, where a is the lattice constant) for each cavity mode, and expressed as $\delta=(\beta^2-\beta_0{}^2)/2\beta_0$, α is the corresponding threshold gain.

By solving eqn (2.39a-e), a cavity frequency ν for each band-edge mode and the corresponding threshold gain α for a given set of coupling coefficients, κ_1, κ_2, and κ_3, can be obtained. When only the cavity mode frequencies are required, the derivation terms and the threshold gain α in eqn (2.39a-e) can be set to zero, and the individual cavity frequencies can then be derived as follows:

$$\nu_1 = \frac{c}{2\pi neff}(\beta_0 - \kappa_1 - \kappa_2 + \kappa_3) \tag{2.40a}$$

$$\nu_2 = \frac{c}{2\pi neff}(\beta_0 - \frac{1}{2}\kappa_1 + \frac{1}{2}\kappa_2 - \kappa_3) \tag{2.40b}$$

$$\nu_3 = \frac{c}{2\pi neff}(\beta_0 + \kappa_1 - \kappa_2 - \kappa_3) \tag{2.40c}$$

$$\nu_4 = \frac{c}{2\pi neff}(\beta_0 + \frac{1}{2}\kappa_1 + \frac{1}{2}\kappa_2 + \kappa_3) \tag{2.40d}$$

where, c is the velocity of a photon in vacuum, and n_{eff} is the effective refractive index of the device structure. There are four cavity mode frequencies, $\nu_1 - \nu_4$, which correspond to the four band-edge, including two degenerate modes ν_2 and ν_4. Once the cavity mode frequency at the individual band-edges can be obtained, we can derive the coupling coefficients κ_1, κ_2, and κ_3 from eqn (2.40a-d) as follows:

$$\kappa_1 = \frac{-\nu_1 - \nu_2 + \nu_3 + \nu_4}{\nu_1 + 2\nu_2 + \nu_3 + 2\nu_4} 2\beta_0 \tag{2.41a}$$

$$\kappa_2 = \frac{-\nu_1 + \nu_2 - \nu_3 + \nu_4}{\nu_1 + 2\nu_2 + \nu_3 + 2\nu_4} 2\beta_0 \tag{2.41b}$$

$$\kappa_3 = \frac{\nu_1 - 2\nu_2 - \nu_3 + 2\nu_4}{\nu_1 + 2\nu_2 + \nu_3 + 2\nu_4} 2\beta_0 \tag{2.41c}$$

By comparing the value of coupling coefficients κ_1, κ_2, and κ_3 based on actual device parameters, we can determine which kind of DFB mechanism provide the major significant contribution to support the lasing oscillation.

II. K2 numerical results

The 2D PC structure investigated here consists of an infinite triangular lattice with circular air holes in the x and y directions, as shown in Fig 2.6. The structure is assumed to be uniform in the z direction. We don't consider the gain effects during calculation. While considering infinite structure, the magnetic field can be described by the Bloch mode [14],

$$Hz(r) = \sum_G h_G \exp\left[j(k+G)\cdot r\right] \tag{2.34}$$

where $$Hz = H_1 e^{-i\beta 0\hat{x}} + H_2 e^{-i\beta 0(\frac{-1}{2}\hat{x}+\frac{\sqrt{3}}{2}\hat{y})} + H_3 e^{-i\beta 0(\frac{-1}{2}\hat{x}-\frac{\sqrt{3}}{2}\hat{y})} \quad (2.42)$$

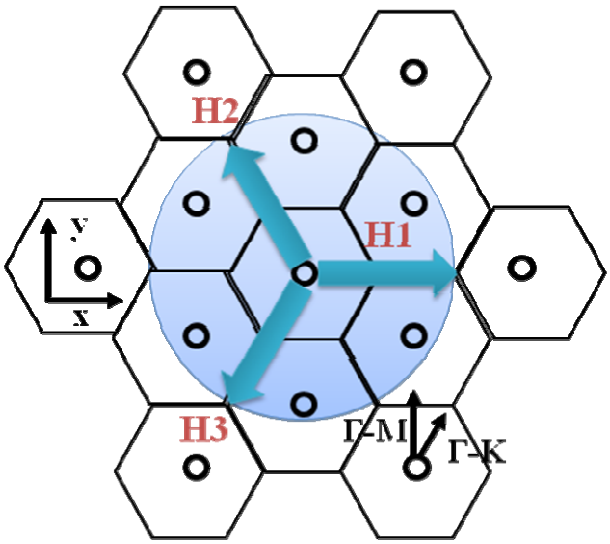

Figure 2.6 Schematic diagram of three propagation waves in triangular lattice for K2 point

put eqn (2.42) and eqn (2.31) into the wave eqn (2.30), and comparing the equal exponential terms, we obtain three wave equations :

$$-\frac{\partial}{\partial x}H_1 + (-\alpha - i\delta)H_1 = i\frac{\kappa}{2}(H_2 + H_3) \quad (2.43a)$$

$$-\frac{1}{2}\frac{\partial}{\partial x}H_2 - \frac{\sqrt{3}}{2}\frac{\partial}{\partial y}H_2 + (-\alpha - i\delta)H_2 = i\frac{\kappa}{2}(H_1 + H_3) \quad (2.43b)$$

$$\frac{1}{2}\frac{\partial}{\partial x}H_3 + \frac{\sqrt{3}}{2}\frac{\partial}{\partial y}H_3 + (-\alpha - i\delta)H_3 = i\frac{\kappa}{2}(H_1 + H_2) \quad (2.43c)$$

where, H_1, H_2, H_3 express the envelope magnetic field distributions of individual light waves propagating in the three equivalent Γ-K directions: 0°, 120°, 240° with respect to the x axis. κ is the coupling coefficient between light waves propagating at 120° to each other (H_1 and H_2, H_2 and H_3, H_1 and H_3), δ is the deviation of the wave number β (expressed as $2\pi\nu/c$, where ν is the frequency and c is the velocity of light) from the fundamental propagation constant β_0 (equal to $8\pi/3a$, where a is the lattice constant) for each cavity mode, and expressed as $\delta = (\beta^2 - {\beta_0}^2)/2\beta_0$, α is the corresponding threshold gain.

By solving eqn (2.43a-c), a cavity frequency ν for each band-edge mode and the corresponding threshold gain α for a given set of coupling coefficients, κ can be obtained. When only the cavity mode frequencies are required, the derivation terms and the threshold gain α in eqn (2.39a-e) can be set to zero, and the individual cavity frequencies can then be derived as follows:

$$\nu 1 = \frac{c}{2\pi neff}(\beta 0 - \kappa) \tag{2.44a}$$

$$\nu 2 = \frac{c}{2\pi neff}(\beta 0 + \frac{1}{2}\kappa) \tag{2.44b}$$

where, c is the velocity of a photon in vacuum, and n_{eff} is the effective refractive index of the device structure. There are two cavity mode frequencies, ν_1, ν_2 , which correspond to the two band-edge, including one degenerate modes ν_2. Once the cavity mode frequency at the individual band-edges can be obtained, we can derive the coupling coefficients κ from eqn (2.44a,b) as follows:

$$\kappa = \frac{\nu_2 - \nu_1}{\nu_1 + 2\nu_2} 2\beta_0 \tag{2.45}$$

From the 2D couple-wave model, we know light at K2 band-edge can couple to each other and form the triangular feedback close loop via DFB effect.

III. M3 numerical results

The 2D PC structure investigated here consists of an infinite triangular lattice with circular air holes in the x and y directions, as shown in Fig 2.7. The structure is assumed to be uniform in the z direction. We don't consider the gain effects during calculation. While considering infinite structure, the magnetic field can be described by the Bloch mode [14],

$$Hz(r) = \sum_G h_G \exp\left[j(k+G)\cdot r\right] \tag{2.34}$$

where $$Hz = H_1 + H_2 + H_3 + H_4 \tag{2.46}$$

note that here we already know the angle between two propagating waves are.

Actually we can easily derive the couple-wave equations. Therefore, the phase term will not describe in detail.

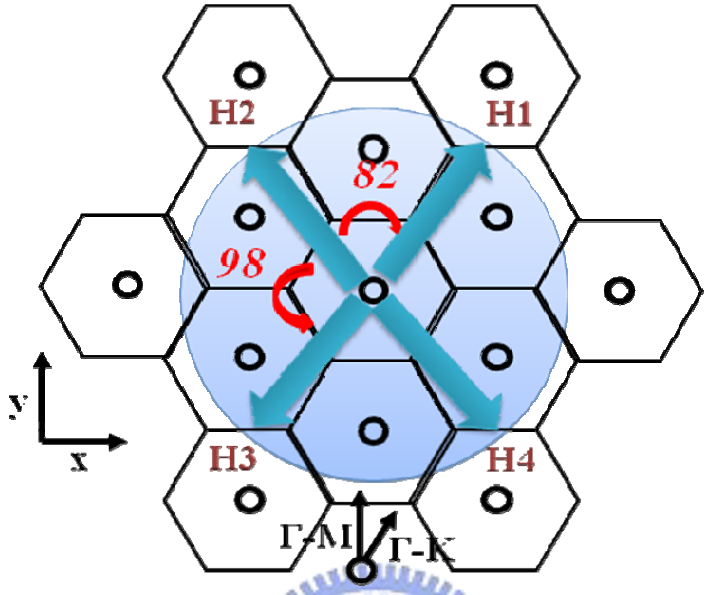

Figure 2.7 Schematic diagram of four propagation waves in triangular lattice for M3 point

put eqn (2.46) and eqn (2.31) into the wave eqn (2.30), and comparing the equal exponential terms, we obtain four wave equations :

$$(\beta_0 - \delta)H_1 = -\kappa_1 H_2 + +\kappa_3 H_3 + \kappa_2 H_4 \quad (2.47a)$$

$$(\beta_0 - \delta)H_2 = -\kappa_1 H_1 + \kappa_2 H_3 + \kappa_3 H_4 \quad (2.47b)$$

$$(\beta_0 - \delta)H_3 = \kappa_3 H_1 + \kappa_2 H_2 - \kappa_1 H_4 \quad (2.47c)$$

$$(\beta_0 - \delta)H_4 = \kappa_2 H_1 + \kappa_3 H_2 + \kappa_1 H_3 \quad (2.47d)$$

where, H_1, H_2, H_3, H_4 express the envelope magnetic field distributions of individual light waves propagating in the four directions: κ_1, κ_2, and κ_3 are the coupling coefficients between light waves propagating at 82° to each other (H_1 and H_2, H_3 and H_4), at 98° (H_1 and H_4, H_2 and H_3), and at 180° (H_1 and H_3, H_2 and H_4), respectively. δ is the deviation of the wave number β (expressed as $2\pi\nu$/c, where ν is the frequency and c is the velocity of light) from the fundamental propagation constant β_0 (equal to $4.7\pi/\sqrt{3}a$, where a is the lattice constant) for each cavity mode, and

expressed as $\delta = (\beta^2 - \beta_0{}^2)/2\beta_0$, α is the corresponding threshold gain

By solving eqn (2.47a-d), a cavity frequency ν for each band-edge mode and the corresponding threshold gain α for a given set of coupling coefficients, κ_1, κ_2, and κ_3, can be obtained. When only the cavity mode frequencies are required, the derivation terms and the threshold gain α in eqn (2.39a-e) can be set to zero, and the individual cavity frequencies can then be derived as follows:

$$\nu_1 = \frac{c}{2\pi neff}(\beta_0 + \kappa_1 - \kappa_2 - \kappa_3) \tag{2.48a}$$

$$\nu_2 = \frac{c}{2\pi neff}(\beta_0 - \kappa_1 + \kappa_2 - \kappa_3) \tag{2.48b}$$

$$\nu_3 = \frac{c}{2\pi neff}(\beta_0 - \kappa_1 - \kappa_2 + \kappa_3) \tag{2.48c}$$

$$\nu_4 = \frac{c}{2\pi neff}(\beta_0 + \kappa_1 + \kappa_2 + \kappa_3) \tag{2.48d}$$

where, c is the velocity of a photon in vacuum, and n_{eff} is the effective refractive index of the device structure. There are four cavity mode frequencies, $\nu_1 - \nu_4$, which correspond to the four band-edge. Once the cavity mode frequency at the individual band-edges can be obtained, we can derive the coupling coefficients κ_1, κ_2, and κ_3 from eqn (2.40a-d) as follows

$$\kappa_1 = \frac{\nu_1 - \nu_2 - \nu_3 + \nu_4}{\nu_1 + \nu_2 + \nu_3 + \nu_4}\beta_0 \tag{2.49a}$$

$$\kappa_2 = \frac{-\nu_1 + \nu_2 - \nu_3 + \nu_4}{\nu_1 + \nu_2 + \nu_3 + \nu_4}\beta_0 \tag{2.49b}$$

$$\kappa_3 = \frac{-\nu_1 - \nu_2 + \nu_3 + \nu_4}{\nu_1 + \nu_2 + \nu_3 + \nu_4}\beta_0 \tag{2.49c}$$

By comparing the value of coupling coefficients κ_1, κ_2, and κ_3 based on actual device parameters, we can determine which kind of DFB mechanism provide the most significant contribution to support the lasing oscillation.

So far, the couple-wave model for different band-edge has been established. For next section, Bragg diffraction in different band-edge will be discussed to confirm the 2D

model we formed.

2.4 Bragg diffraction in 2D triangular lattice [17,18]

Fig 2.8a shows a band diagram of a triangular-lattice photonic crystal. The points I, II, and III are the points Γ_1, M_1, and K_1, respectively. The reciprocal space of the structure is a space combined by hexagons. Fig 2.8b shows a schematic diagram of a reciprocal space. The $\mathbf{K_1}$ and $\mathbf{K_2}$ are the Bragg vectors with the same magnitude, $|K|=2\pi/a$, where a is the lattice constant of the photonic crystal. Consider the TE modes in the 2-D photonic crystal structure, the diffracted light wave from the structure must satisfy the relationship:

$$k_d = k_i + q_1 K_1 + q_2 K_2, \qquad q_{1,2} = 0, \pm 1, \pm 2, \ldots \tag{2.21}$$

$$\omega_d = \omega_i \tag{2.22}$$

where k_d is xy-component wave vector of diffracted light wave, k_i is xy-component wave vector of incident light wave, $q_{1,2}$ is order of coupling, ω_d is the frequency of diffracted light wave, and ω_i is the frequency of incident light wave.

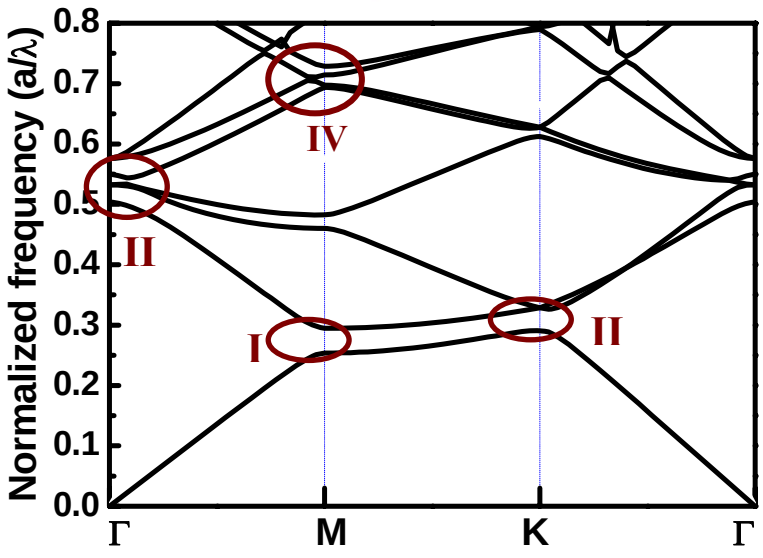

Figure 2.8a The band diagram of a triangular lattice photonic crystal

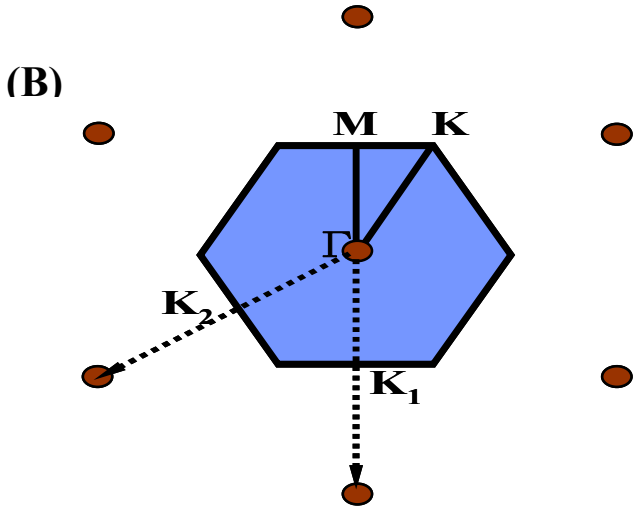

Figure 2.8b The schematic diagram of a reciprocal space

It is expected lasing occurs at specific points on the Brillouin-zone boundary (Γ, M, and K) and at the points at which bands cross and split. At these lasing points, waves propagating in different directions couple to significantly increase the mode density. It is particularly interesting that each of these points exhibits a different type of wave coupling. For example, as shown in Fig 2.9a, the coupling at point I only involves two waves, propagating in the forward and backward directions. This coupling is similar to that of a conventional DFB laser. However, there can be six equivalent Γ-M directions in the structure; that is, the cavity can exist independently in each of the three different directions to form three independent lasers. Point II has a unique coupling characteristic unachievable in conventional DFB lasers, the coupling of waves propagating in three different directions as shown in Fig 2.9b. This means the cavity is a triangular. In fact, there can also be six Γ-K directions in the structure; therefore, two different lasing cavities in different Γ-K directions coexist independently. At point III the coupling includes waves in in-plane all six directions; 0°, 60°, 120°, -60°, -120°, and 180° as shown in Fig 2.9c. In addition, the coupled light can be emitted perpendicular from the surface according to first order Bragg diffraction, as shown in Fig 2.10. This is the same phenomenon that occurs in conventional grating-coupled surface-emitting lasers.

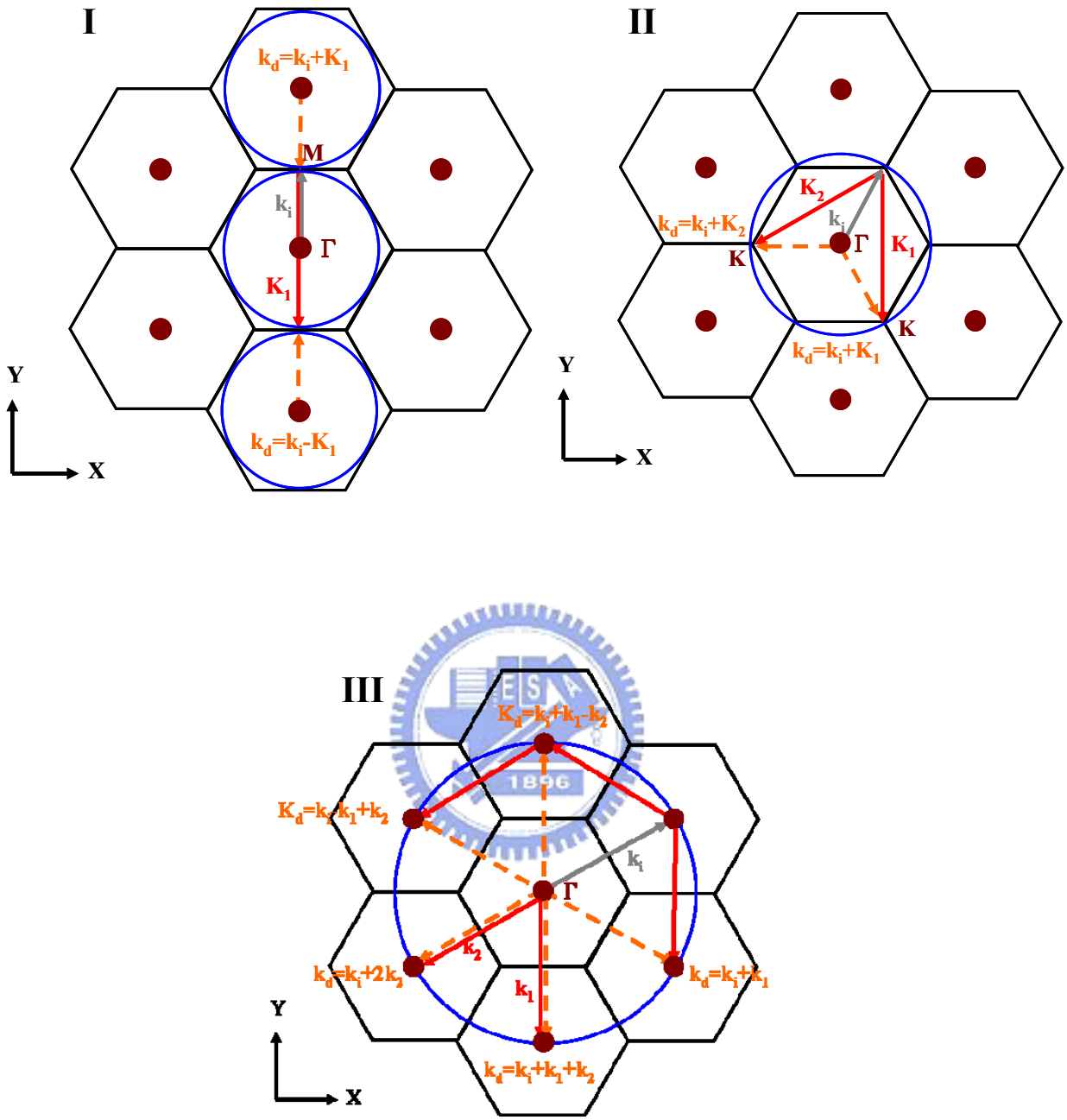

Figure 2.9 Wave vector diagram at (A) point I (B) point II (C)point III ,

ki and kd indicate incident and diffracted light wave

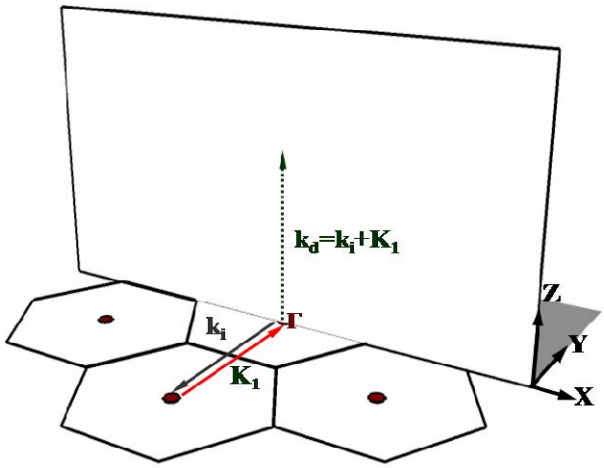

Figure 2.10 The wave vector diagram at point III in vertical direction

The device, therefore, functions as a surface emitting lasers. Fig 2.11a and Fig 2.11b show the in-plane and vertical diffraction at point IV. In this case, the light wave is diffracted in five Γ-K directions and in the vertical direction similar to point III, and Ki+q1K1+q2K2 reaches the six Γ' points. Fig 2.11c shows the wave-vector diagram of one Γ' point where the light wave is diffracted in an oblique direction. The light wave is also diffracted in a bottom oblique direction. The same diffraction phenomena occur at the other five G8 points, resulting in diffraction in 19 directions at point IV.

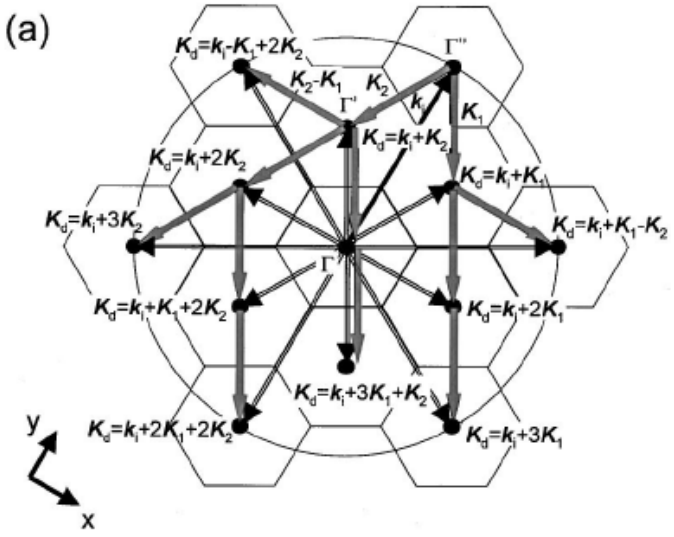

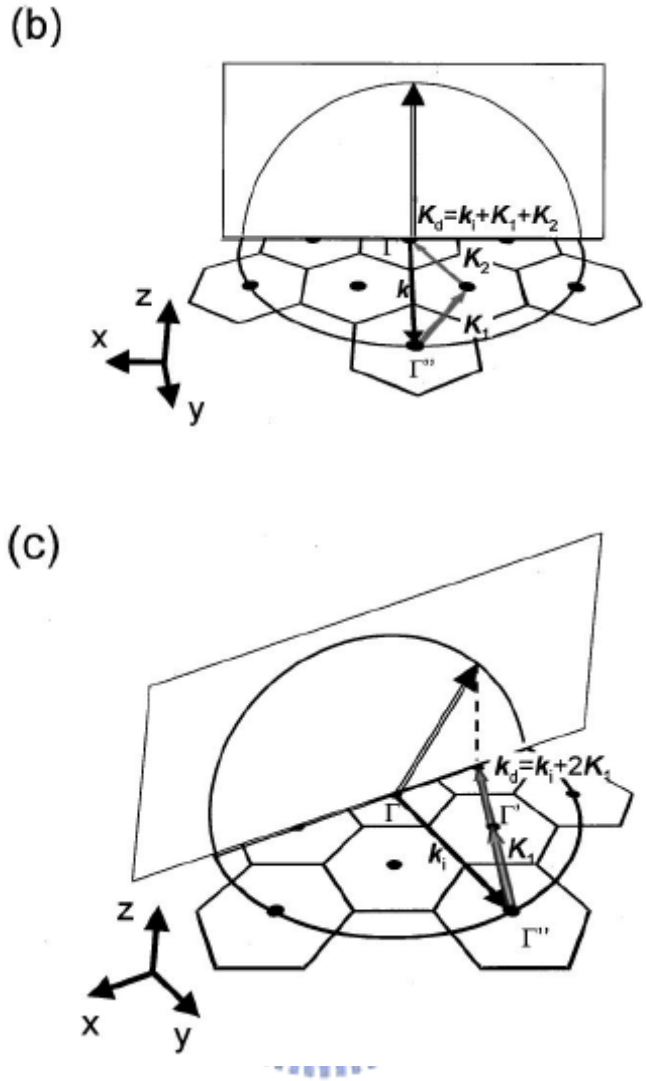

Figure 2.11 Wave vector diagram of (A) in-plane and (B) vertical direction at point IV (C) Wave vector diagram showing diffraction in an oblique direction at point IV.

References

1. M. Imada, S. Noda, A. Chutinan, T. Tokuda, M. Murata, and G. Sasaki, *Appl. Phys .Lett*. **75**, 316 (1999)
2. S. Noda, M. Yokoyama, M. Imada, A. Chutinan, and M. Mochizuki, *Science* **293**, 1123 (2001)
3. H. Y. Ryu, S. H. Kwon, Y. J. Lee, and J. S. Kim, *Appl. Phys. Lett.* **80**, 3467 (2002)
4. G. A. Turnbull, P. Andrew, W. L. Barns, and I. D. W. Samuel, *Appl. Phys. Lett.* **82**, 313 (2003)
5. K. Sakai, E. Miyai, T. Sakaguchi, D. Ohnishi, T. Okano, and S. Noda, *IEEE J. Sel. Areas Commun.* 23, 1335-1340 (2005)
6. M. Imada, A. Chutinan, S. Noda and M. Mochizuki *Phys. Rev. B* **65**, 195306 1-8 (2002)
7. M. Yokoyama and S. Noda *Opt. Express* **13**, 2869-2880 (2005)
8. H. Kogelnik and C. V. Shank *Appl. Phys. Lett.* **43**, 2327-2335 (1972)
9. Distributed Feedback Laser Diodes and Optical Tunable Filters
10. Streifer, W., Burnham, R.D.and Scifres, D.R. *IEEE J. Quantum Electron.* **QE11**(4), 154-161 (1975).
11. David, K. *IEEE J. Quantum Electron.***27**(6), 1714-1724, 1991
12. Kyosuke Sakai, Eiji Miyai and Susumu Noda *Optics Express* Vol. **15**, 3981, (2007)
13. Kyosuke Sakai, Eiji Miyai and Susumu Noda *APL* , **89**, 021101 (2006)
14. Plihal and A. A. Maradudin, *Phys. Rev. B,* **44**, 8565 (1991)
15. H. Kogelnik, Bell Syst. Tech. J. **48**, 2909 (1969)
16. T. Ochiai and K.Sakoda *Phys. Rev. B* **63**, pp. 125 107-1-125 107-7, (2001)
17. M. Imada, A. Chutinan, S. Noda, M. Mochizuki, *Phy. Rev. B*, 65, 195306 (2002)

18. M. Notomi, H. Suzuki, and T. Tamamura, *Appl. Phys. Lett.*, **78**, 1325 (2001)

Chapter 3

Fabrication of Nitride-based 2D Photonic Crystal Surface Emitting Lasers

Introduction

Currently, photonic crystals, which are periodic patterns with sizes of sub-micrometer, are usually fabricated using electron-beam lithography. The electron-beam lithography (EBL) is a technique using electron beam to generate patterns on a surface with a resolution limited by De Broglie relationship ($\lambda < 0.1$ nm for 10-50 KeV electrons), which is far smaller than the light diffraction limitation. Therefore, it can beat the diffraction limit of light to create a pattern which only has a few nanometers line-width without any mask. The first EBL machine, based on SEM system, was developed in the 1960s. The EBL system usually consists of an electron gun for generating electron beam, a beam blanker for controlling the electron beam, electron lenses for focusing the electron beam, a stage and a computer control system as shown in Fig 3.1.

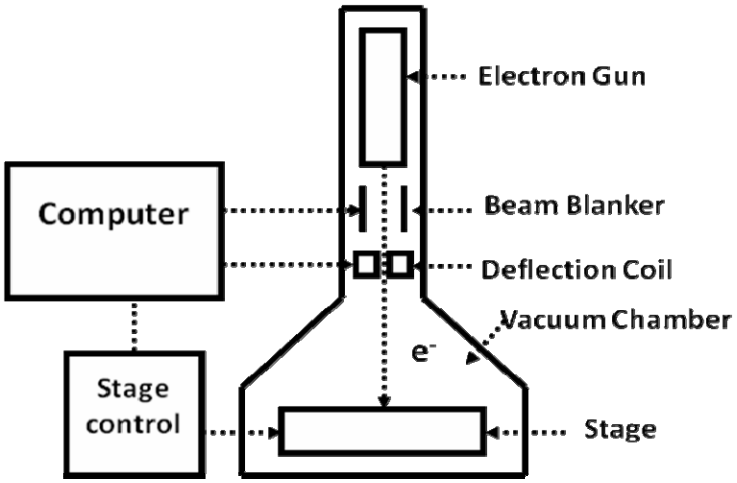

Figure 3.1 The typical schematic diagram of EBL system

3.1 Wafer Preparation

The nitride heterostructure of GaN-based MCLED was grown by metal-organic chemical vapor deposition (MOCVD) system (EMCORE D-75) on the polished optical-grade c-face (0001) 2” diameter sapphire substrate, as shown in Fig. 3.2a. Trimethylindium (TMIn), Trimethylgallium (TMGa), Trimethylaluminum (TMAl), and ammonia (NH_3) were used as the In, Ga, Al, and N sources, respectively. Initially, a thermal cleaning process was carried out at 1080°C for 10 minutes in a stream of hydrogen ambient before the growth of epitaxial layers. The 30nm thick GaN nucleation layer was first grown on the sapphire substrate at 530°C, then 2μm thick undoped GaN buffer layer was grown on it at 1040°C. After that, a 35 pairs of quarter-wave GaN/AlN structure was grown at 1040°C under the fixed chamber pressure of 100Torr and used as the high reflectivity bottom DBR. Finally, the 5λ active pn-junction region was grown atop the GaN/AlN DBR, composed typically of ten $In_{0.2}Ga_{0.8}N$ quantum wells (L_W=2.5 nm) with GaN barriers (L_B=7.5 nm), and surrounded by 560nm thick Si-doped n-type GaN and 200nm thick Mg-doped p-type GaN layers. The reflectivity spectrum of the half structure with 35 pairs of GaN/AlN DBR structure was measured by the n&k ultraviolet-visible spectrometer with normal incident at room temperature, as shown in Fig. 3.2.b The reflectivity spectrum centered at 430nm and stopband width of about 28nm. Fig. 3.2.c shows the PL spectrum of our as grown sample.

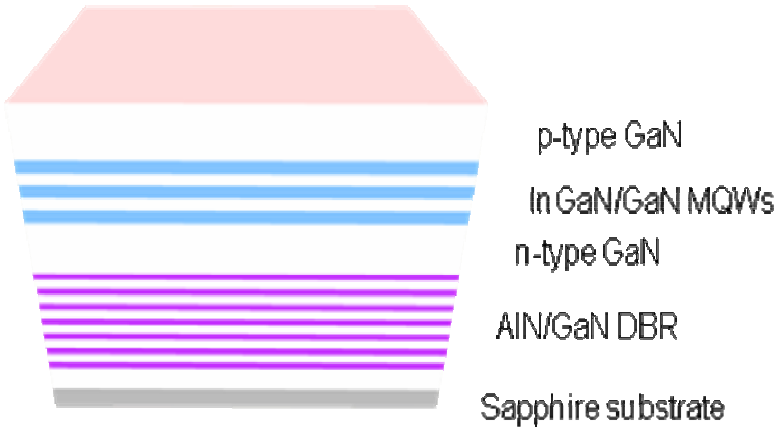

Figure 3.2a The 2D schematic diagram of nitride structure grown by MOCVD

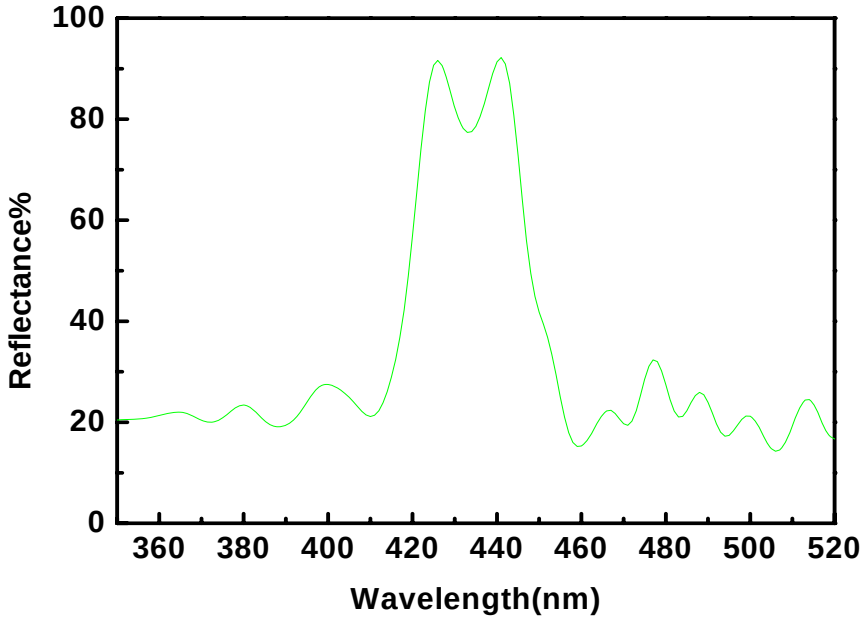

Figure 3.2b Reflectivity spectrum of the half structure with 35 pairs of GaN/AlN DBR structure measured by N&K ultraviolet-visible spectrometer with normal incident at room temperature.

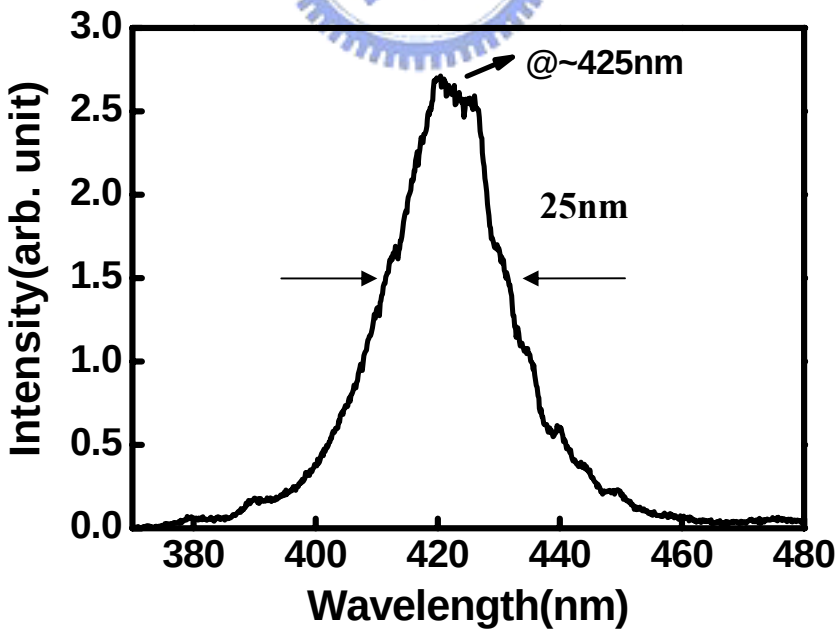

Figure 3.2c The u-PL spectrum of as-grown sample

3.2 Process Procedure

There are some principles to fabricate GaN-based PCSELs, including initial clean (I.C.), plasma enhanced chemical vapour deposition (PECVD) technique, EBL technique and inductively coupled plasma - reactive ion etching (ICP-RIE) technique. The purpose of the I.C. is to remove the small particle and organism on the sample surface. The steps of I.C. are described as below.

Initial clean (I.C.)

1. Degreasing particles in acetone (ACE) 5min by ultrasonic baths.
2. Dipping in isopropyl alcohol (IPA) 5min by ultrasonic baths for organism removed.
3. Rising in de-ionized water (D.I. water) 5min for surface clean.
4. Blowing with N_2 gas for surface drying.
5. Baking by hot plate 120^{o}C, 5min, for wafer drying.

PECVD (SAMCO PD220)

The purpose of PECVD technique is to deposit a SiN film for hard mask. The details of PECVD parameters are expressed as below.

1. Initial clean
2. SiN film deposition :

   $SiHl_4$/Ar : 20sccm

   NH_3 : 10sccm

   N_2 : 490sccm

   Temperature : 300℃

   RF power : 35W

   Pressure :100Pa

   Time : 20min for depositing SiN 200nm

EBL

The purpose of the EBL is to define the PC pattern on the photoresist (PMMA) (soft mask). In the process of EBL, a special positive photoresist PMMA (A3) was used. These EBL parameters are described as below.

1. Spin coating use the photoresist : PMMA (A3).
   a. first step : 1000 rpm for 10sec.
   b. second step : 5000 rpm for 90sec.

2. Hard bake : hot plate 180^{o}C, 1hr.
3. Exposure :
   Beam voltage : 10KeV
   Writefield size : 50μm
4. Development : dipping in IPA : MIBK(3 : 1) 50sec.
5. Fixing : rising in IPA 30sec.
6. Blowing with N_2 gas for drying.
7. Hard bake : hot plate 120^{o}C, 4min.

ICP-RIE (Oxford Plasmalab system 100)

The soft mask was transfered to SiN film to form the hard mask by using ICP-RIE. These ICP-RIE techniques are described as below.

1. SiN film etching:
   Ar/O_2: 5sccm
   CHF_3: 50sccm
   Forward power: 150W
   Pressure: 7.5*10^{-9}Torr
   Temperature: 20℃
   Time: 100 second for etching SiN film 200nm
2. Initial clean for remove soft mask

ICP-RIE (SAMCO RIE-101PH)

The purpose of the ICP-RIE techique is to form the PC layer on GaN. The hard mask was transferred to GaN by using ICP-RIE techique. Figure 3.3 are shown the SEM image of top view and cross section of completed 2D PCSELs, respectively. These ICP-RIE techniques are described as below.

1. P-GaN etching:
   Ar : 10sccm
   Cl_2 : 25sccm
   ICP power : 200W
   Bias power : 200W
   Pressure : 0.33Pa
2. Dipping BOE 40sec. for remove hard mask

3. Polishing sapphire for optical pumping

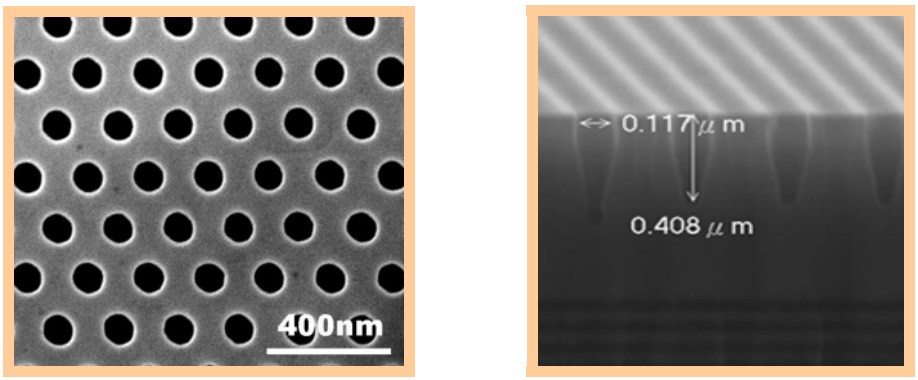

Figure 3.3 SEM image of plane view and cross section

3.3 Process flowchart

The PCSELs was fabricated by following process steps. In the beginning, the hard mask SiN 200nm was deposited by PECVD. Then PMMA layer (150nm) was spun by spinner and exposed using E-beam writer to form soft mask. The pattern on soft mask was transferred to SiN film to form the hard mask by using ICP-RIE (Oxford Plasmalab system 100), and then the PMMA layer was removed by dipping ACE . The pattern on hard mask was transferred to GaN by using ICP-RIE (SAMCO RIE-101PH) to form the PC layer. Finally, the sample dips in BOE to remove the hard mask.

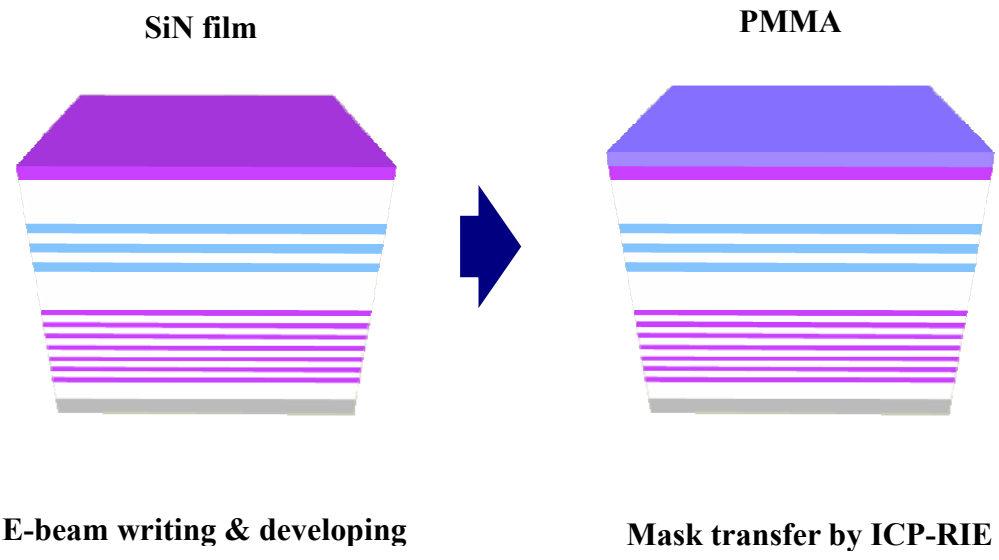

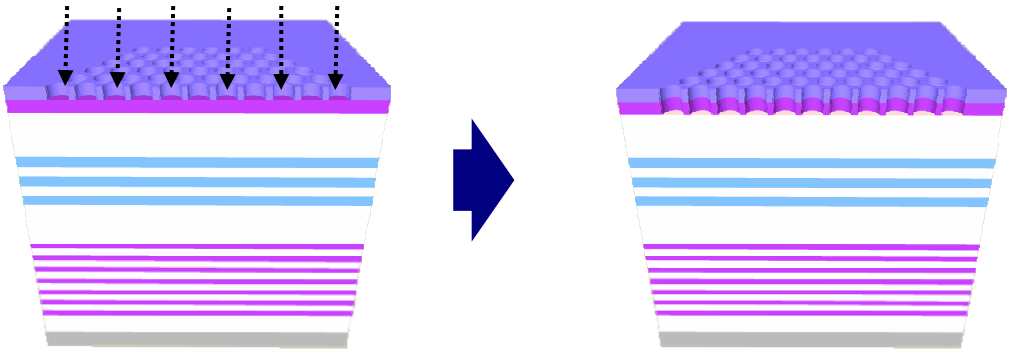

Remove PMMA by acetone **ICP dry etching**

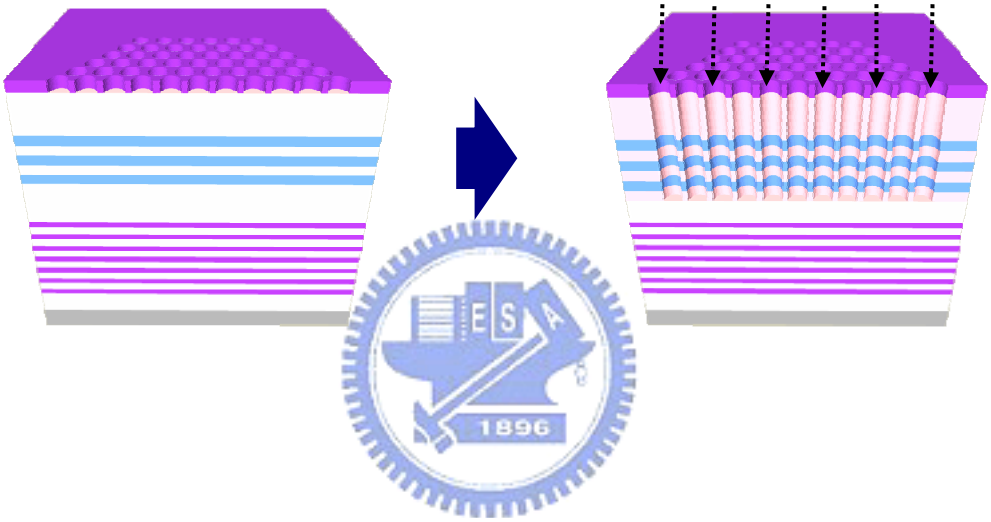

Complete device after removing SiN film

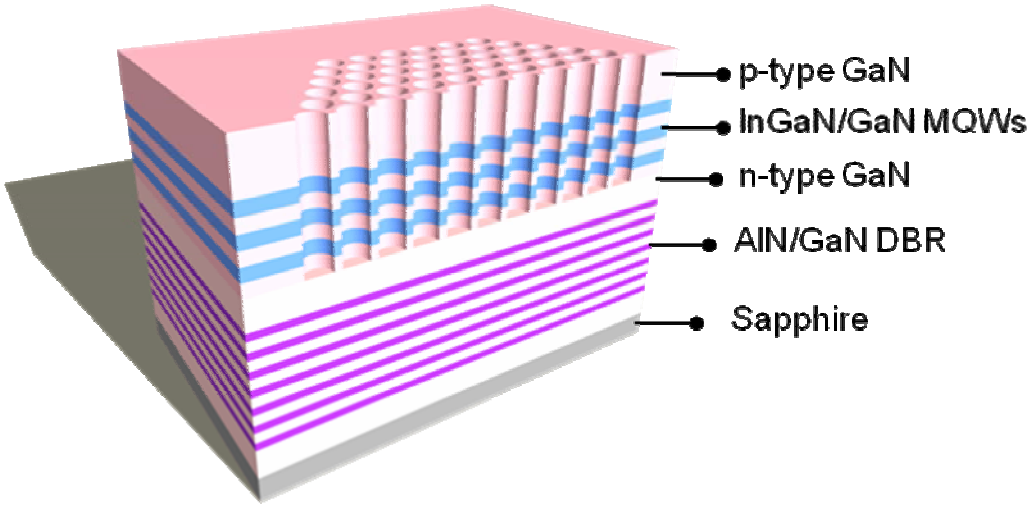

To completely describe the process flowchart, each process conditions are entirely listed in the table.

Step	Process	Conditions
1	Soft mask	(1) I.C. (2) Deposit 200nm SiN by PECVD. (3) Spin 150nm PMMA by spinner (4) Define PCSELs pattern by EBL. (5) Development. (6) Hard bake
2	Hard mask	(1) Dry etching by ICP-RIE (Oxford Plasmalab system 100) to form the hard mask. (2) Remove PMMA by ACE. (3) Hard bake.
3	PCSELs	(1) Dry etching by ICP-RIE ((SAMCO RIE-101PH) to transfer the hard mask to GaN. (2) Remove hard mask by BOE. (3) Hard bake.

Chapter 4

Optical Characteristics of GaN-based 2D Photonic Crystal Surface Emitting Lasers

4.1 The design for PCSELs

In this section, we focus on the design of our GaN-based 2D PCSELs. Initially, we calculate the band diagram with TE like mode to determine the normalized frequency which we choose for specific band-edge groups. Normalized frequency is the ratio of the wavelengths of optical modes to the PC lattice constants. The lasing wavelength could be expected while the lattice constant is determined. The lasing wavelength is located within the emission of the active layer. According to the theory described in chapter 2, 2D periodic structure embedded in the laser could induce Bragg diffraction, which results in Multi-directional coupling. This coupling can effectively increase the Bragg mode density of several band edges, Γ、K and M. The couple wave could emit normally from the sample surface due to the first Bragg diffraction. Therefore, we can design a GaN-based 2D PCSEL operating at the designed lasing wavelength with the optimized lattice constant at Brillouin zone boundary, Γ、K and M point, which can be defined in the photonic band diagram.

In this study, we fabricate several devices with the consistent r/a value (r/a=0.28) and calculate the band diagram of PC using 2D plan wave expansion method (PWEM). In fact, the 2D PWEM couldn't precisely evaluate the photonic band diagram of our 3D structure. That means we should do some modification to parameters describing our structure and then bring them into the 2D PWEM to approximate real condition. Therefore, according to reference [1], we further bring two parameters, confinement factor (Γ_g) and effective refractive index (n_{eff}) into our calculation. Γ_g is the ratio of

the light confined within the 2D PC structure to the light inside the whole device, and n_{eff} is the effective refractive index of the entire device with PC structure. Γ_g and n_{eff} could be used to estimate the effective dielectric constant of nano-hole (ε_a) and the background (ε_b) for 2D PWEM calculation to further approximate the 3-D structure. These two parameters can be obtained by solving the distribution of the optical field in the in-plane direction. The Γ_g and n_{eff} for describing our structure are estimated to be 0.563 and 2.495, respectively. It is first estimated by transfer matrix method and shown in Fig 4.1.

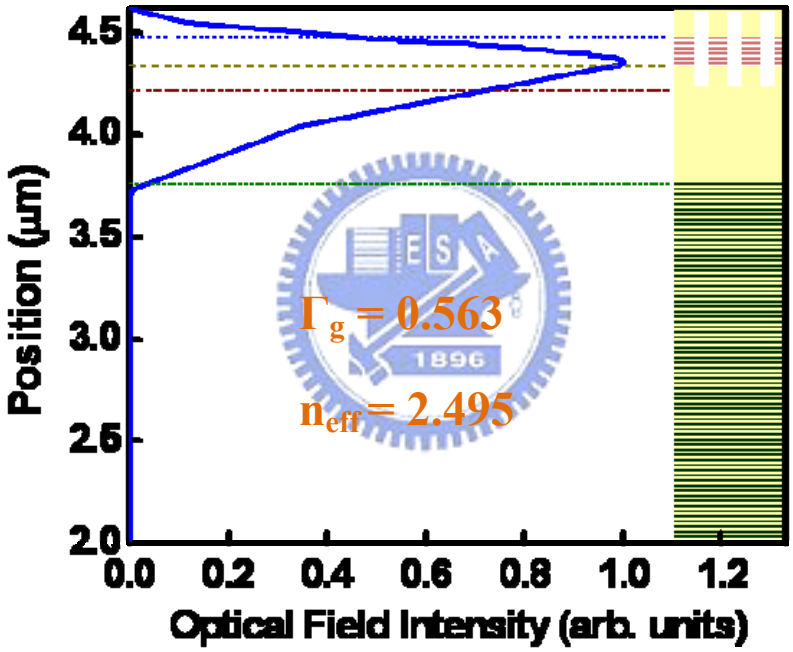

Figure 4.1 The lowest guided mode optical field distribution

Then, we could determine ε_a and ε_b using two conditions:

$$n_{eff}^{\ 2} = f\varepsilon_a + (1-f)\varepsilon_b \tag{4.1}$$

$$\Delta\varepsilon = \varepsilon_b - \varepsilon_a = \Gamma_g(\varepsilon_{mat} - \varepsilon_{air}) \tag{4.2}$$

where the f is a filling factor, ε_{mat} is the dielectric constant of semiconductor, and ε_{air} is the dielectric constant of air. For a triangular lattice PC, f is written as:

$$f = \frac{2\pi r^2}{\sqrt{3}a^2} \tag{4.3}$$

Therefore, the value of ε_a and ε_b in unit cell for our PC device could be obtained to be 4.11 and 7.07, respectively. To bring ε_a and ε_b into the calculation, a band diagram of the 2D triangular lattice PC structure for TE like mode with r/a=0.28 on our sample structure could be estimated as shown in Fig 4.2. It is reasonable to consider only the TE-like mode, we assume that since the carriers in the InGaN layers are confined in the well, they do possess a significant in-plane dipole, which can couple to TE mode. The figure shows that the each mode dispersion curve cross and splits at specific band-edges, the mode density is higher at those boundaries, light at these points can propagate along different direction and have chance to couple and form a laser cavity. According to the theory described in chapter 2, the lasing action of the photonic crystal grating structure could only occur as the Bragg condition is satisfied.

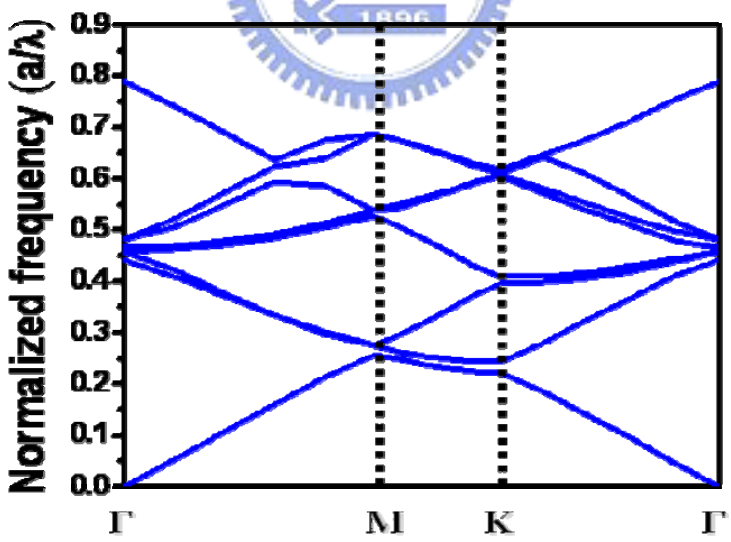

Figure 4.2 The TE band dispersion diagram of our design

In order to have a high probability to meet those modes satisfying Bragg condition, the lattice constant of photonic crystal were determined to range between 190nm to

300nm (the normalized frequency ranges between 0.45 and 0.7) considering a PL peak wavelength of ~425 nm as shown in Fig 3.2.

4.2 Optical pumping system and low temperature system

The optical pumping was performed using a frequency tripled Nd:YVO_4 355nm pulsed laser with a pulse width of ~0.5ns at a repetition rate of 1KHz. The pumping laser beam had a spot size of 50um and was normally incident onto the sample surface covering the whole PC pattern area. The light emission from the sample was collected by a 15X objective lens through a fiber with a 600um core, and couple into a spectrometer with a charge-coupled device (Jobin-Yvon Triax 320 Spectrometer). The spectral resolution is about 0.1nm for spectral output measurement. Fig 4.3 shows the setup of our optical pumping system. The GaN-based PCSELs were placed in a cryogenics controlled chamber for obtaining the characteristic temperature. The temperature of the chamber can be controlled from room temperature 300K down to 100K using the liquid nitrogen as shown in Fig 4.4.

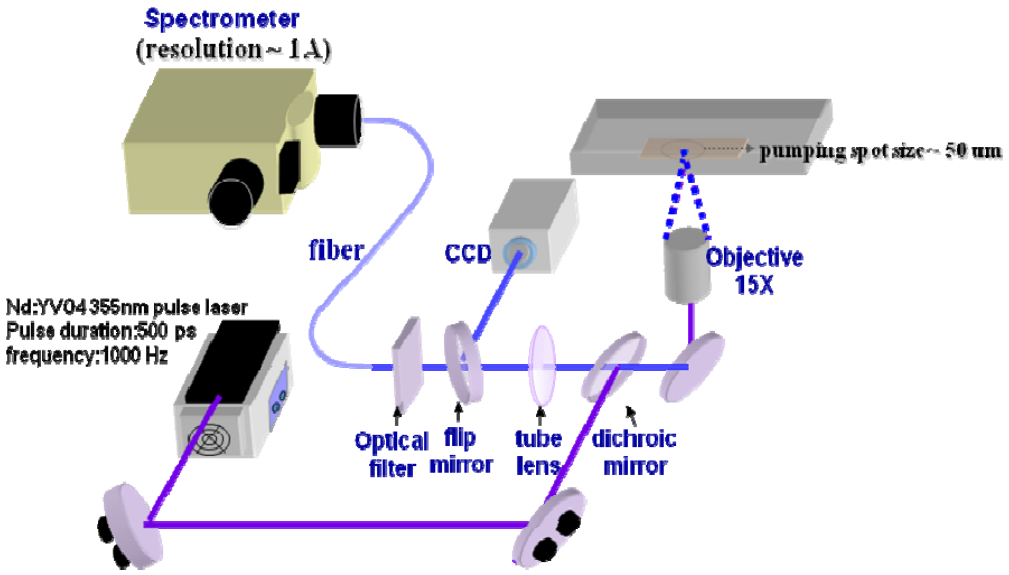

Figure 4.3 The setup of optical pumping system

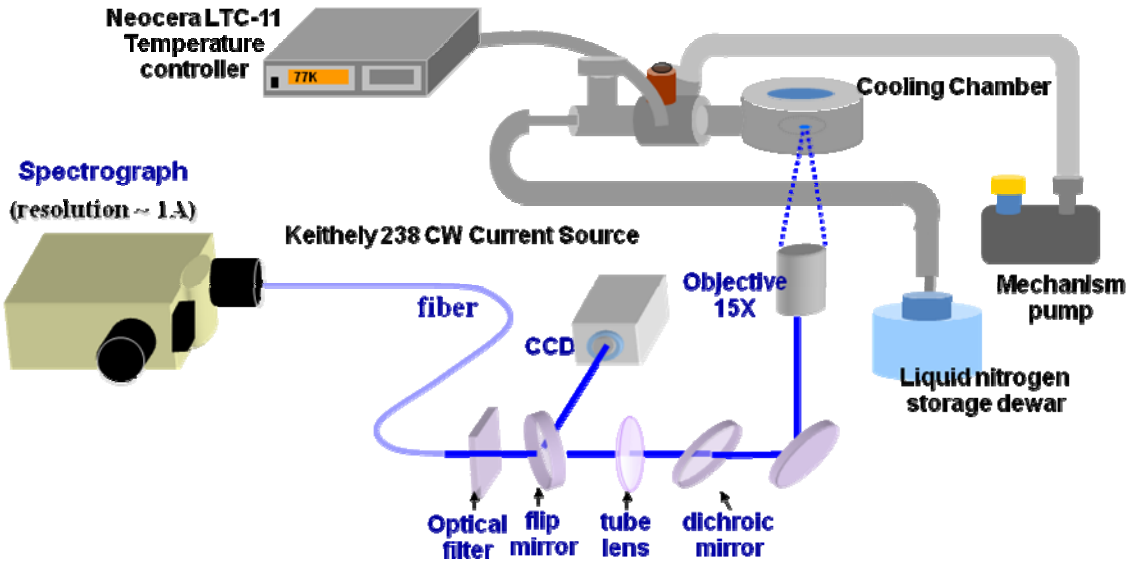

Figure 4.4 The setup of u-PL low temperature system

4.3 Characteristics of GaN-based 2D PCSELs

Threshold

The threshold characteristics of the GaN- based 2D PCSEL were measured using the optical pumping with a pumping spot size of around 50 μm. The lasing action was clearly observed in several different devices with different lasing wavelength from 395 nm to 425 nm. Take the PC lattice constant 254 nm for example. Fig 4.5 shows the output emission intensity as a function of the pumping energy density. The clear threshold characteristic is observed at the threshold pumping energy density of 2.8mJ/cm2. Then the laser output intensity increases abruptly and linearly with the pumping energy above the threshold energy. Fig 4.6 shows the excitation energy dependent emission spectra. These spectra clearly show the transition behavior from spontaneous emission to stimulated emission. Above the threshold, we can observe only one dominant peak wavelength of 419.7nm with a linewidth of 0.19nm.

Moreover, it is interesting to show the emission image below and above the threshold. As the pumping power was below the threshold, the spontaneous emission is uniform above the PC region with a spot size of about 50um. With increasing the pumping power, the stimulated emission occurs over a large area. The lasing area of the GaN-based PCSELs, obtained by a CCD camera which covers almost whole area of PC pattern with only one dominant lasing wavelength. However, Fig 4.5 shows the lasing area is not cover full of the PC region. It could be attributed to the disorder of PC, non-uniformity of pumping laser beam, or inhomogeneiety of InGaN-based gain material. Nevertheless, the nitride based 2D PCSEL could actually have an obviously larger lasing area than that of nitride based VCSEL, which is just several micro-meters.

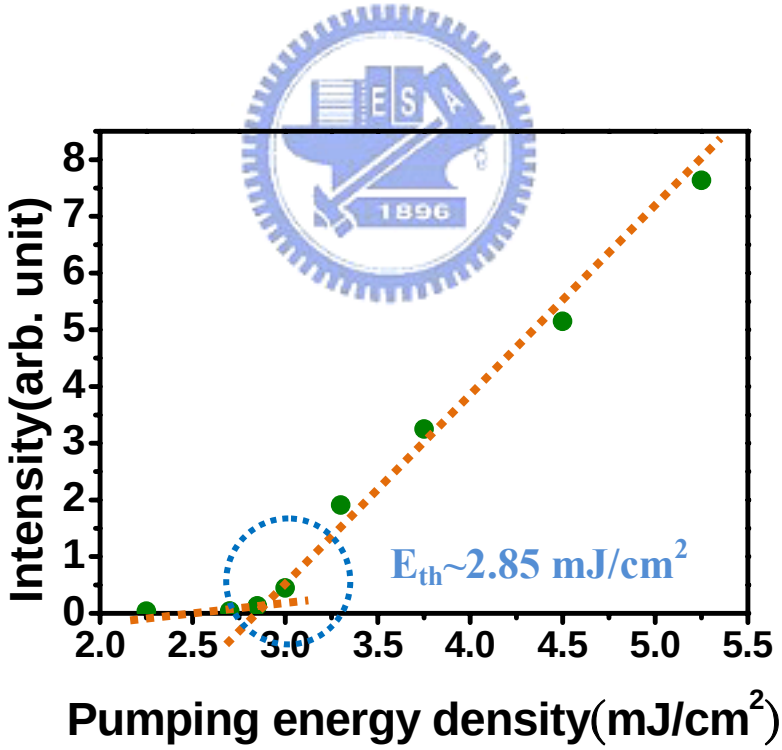

Figure 4.5 The laser intensity versus pumping energy density

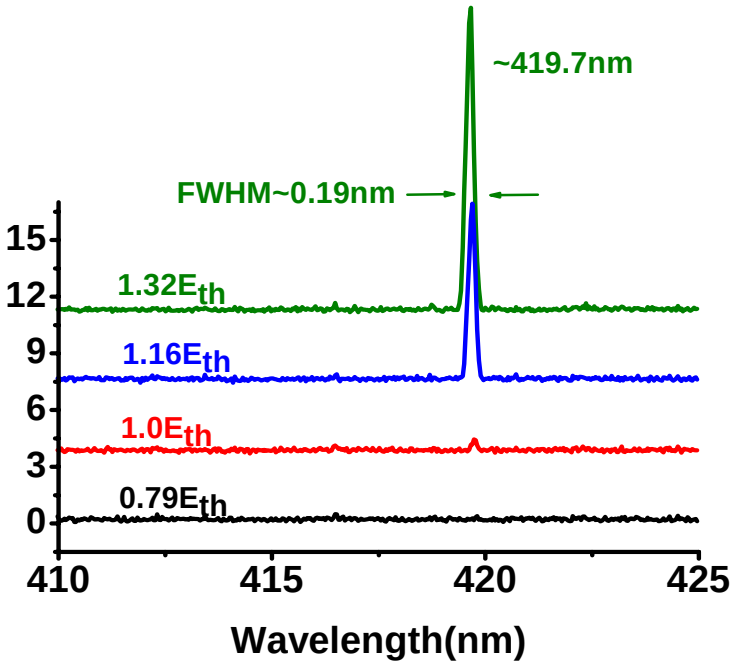

Figure 4.6 Excitation energy density versus emission spectrum

The diagram of normalized frequencies as a function of *r*/*a* ratio is shown in Fig. 4.7. On the other hand, the PWEM in 2D case is being used to consider the effects of partial modal overlap of electromagnetic fields with the PC structures and obtain the band diagram of the hexagonal PC patterns in this structure. The solid (black), dot (red), and dash (green) lines are the calculated band-edge frequencies at the Γ, K and M Brillouin zone boundaries as a function of *r*/*a* ratio, which were in accordance with the measured results.

In order to exam the relationship between lasing wavelength and lattice constant, we plot the normalized frequency $\omega = a/\lambda$ as a function of a in Fig 4.8a , where a is the lattice constant and λ is the lasing wavelength in free space. After normalization, it can be seen clearly that lasing occurs at several normalized frequencies. We also plot the corresponding photonic band structure of 2D triangular photonic crystal using the same normalized frequency in Fig 4.8b Comparing the Fig 4.8a with Fig 4.8b it is

clearly seen that the normalized frequency ω precisely coincides with the three band-edge frequencies (Γ1, K2, M3), indicating that the lasing action could only occur at the specific normalized frequencies that satisfy the Bragg condition. Furthermore, we can confirm the laser operation is provided by multidirectional distributed feedback in the 2D case. The characteristics of Γ1, K2, M3 points lasing can be further identified by the polarization angle of the output beam emission, which will discussed in next section. Note that the output intensity is higher when some of the lasing frequencies are in the stopband of DBR, which could be due to that the bottom DBR here could be treated as a high reflectivity reflector, facilitating top emission efficiency.

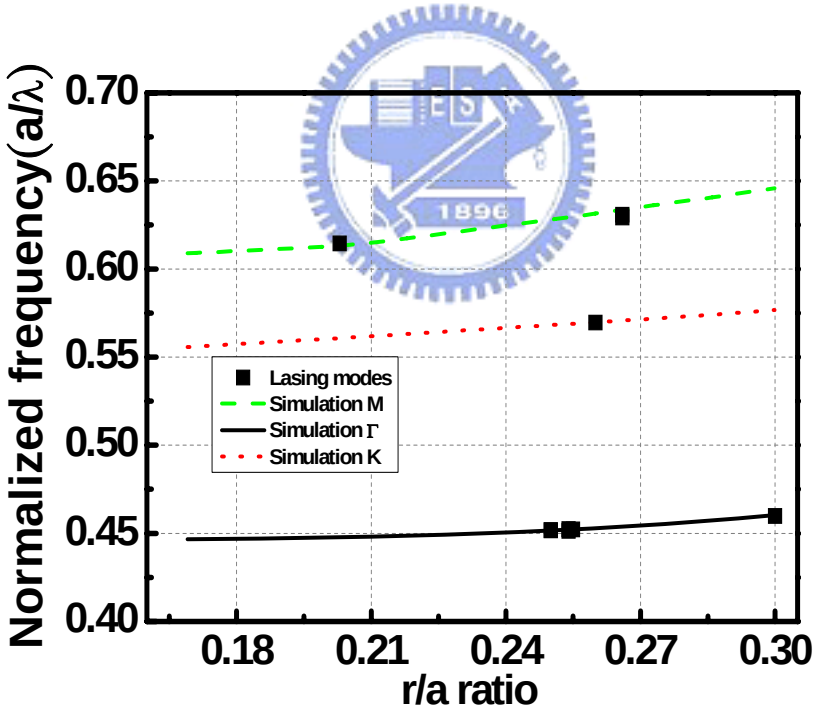

Figure 4.7 Normalized frequency (ω = a/λ) as a function of r/a

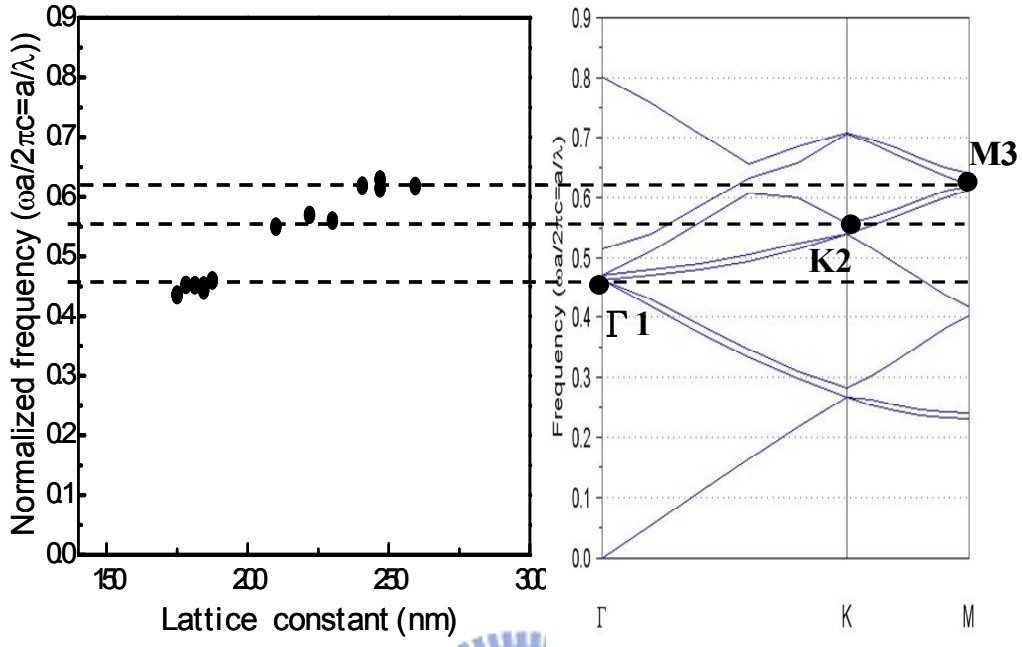

Figure 4.8 (a) Normalized frequency (ω = a/λ) versus lattice constant (b) Photonic band structure of 2D hexagonal photonic crystal

Polarization

The polarization of the laser was measured by inserting and rotating a polarizer in front of a fiber which collects light into a spectrometer. Fig 4.9 shows the laser emission intensity as a function of the angle of the polarizer. Here, defined the degree of polarization (DOP) as DOP = $(I_{max}-I_{min})/(I_{max}+I_{min})$, where I_{max} is the maximum intensity and I_{min} is the minimum intensity. From the figure, the laser degree of polarization was estimated to be about 53%. In fact, the calculation of electric-field vectors in triangular lattice PCs was reported [2], and results suggested that this kind of the laser has weightless polarization property of the laser emission. This could explain the low DOP of our lasers.

It is expected that the lasing oscillation directions are different at different band-

edges based on 2D DFB theory described in Chapter 2. Therefore, in order to confirm the identification of lasing modes, we measured the polarization states of each band-edge, including Γ , K and M. To forecast each polarization states, we draw the laser oscillation direction of each band-edge for triangular lattice in Brillouin zone as shown in Fig 4.10. For TE like mode, it is expected that the polarization direction is orthogonal to the laser oscillation. Once the fabrication process occur structural imperfection or asymmetry, which can be the path for laser beam to diffract normal to PC surface. Therefore, the laser polarization states can be measured by spectrometer. It is noted that all the PC structure are aligned in the same direction which can be seen on the CCD. The measured results of polarization states for different band-edge are plotted in Fig 4.11. It is explicitly show that the polarization states direction are closely matched to Fig 4.10 we draw, which is a clear evidence to prove the existence of the lasing modes correspond to specific band-edges.

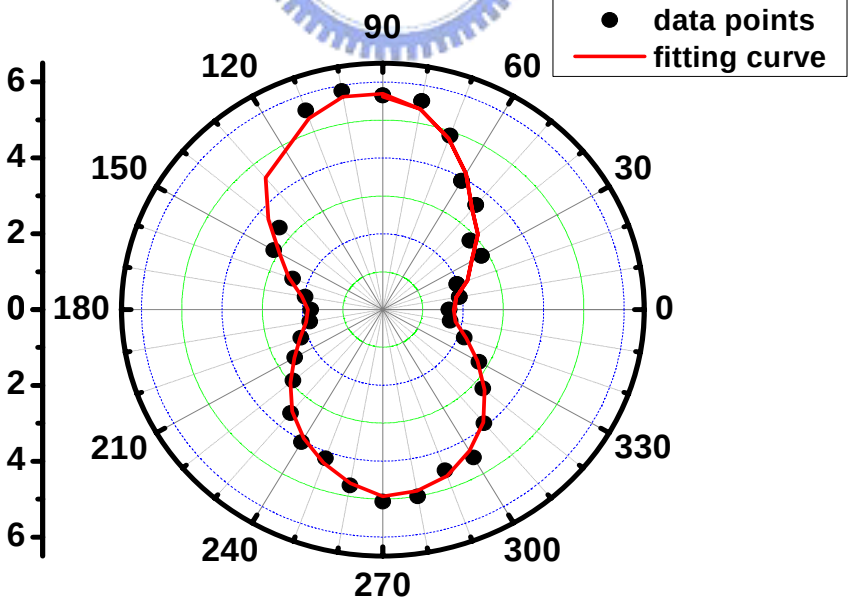

Figure 4.9 The degree of polarization state

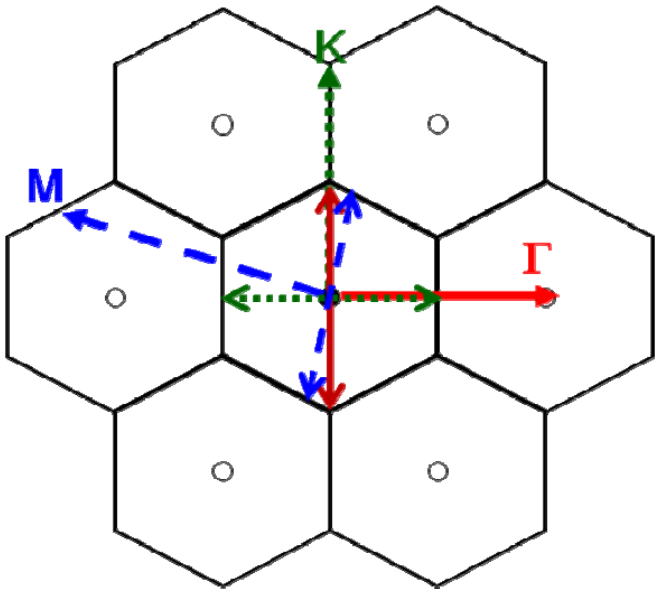

Figure 4.10 The lasing oscillation for Γ K M band-edge in K space

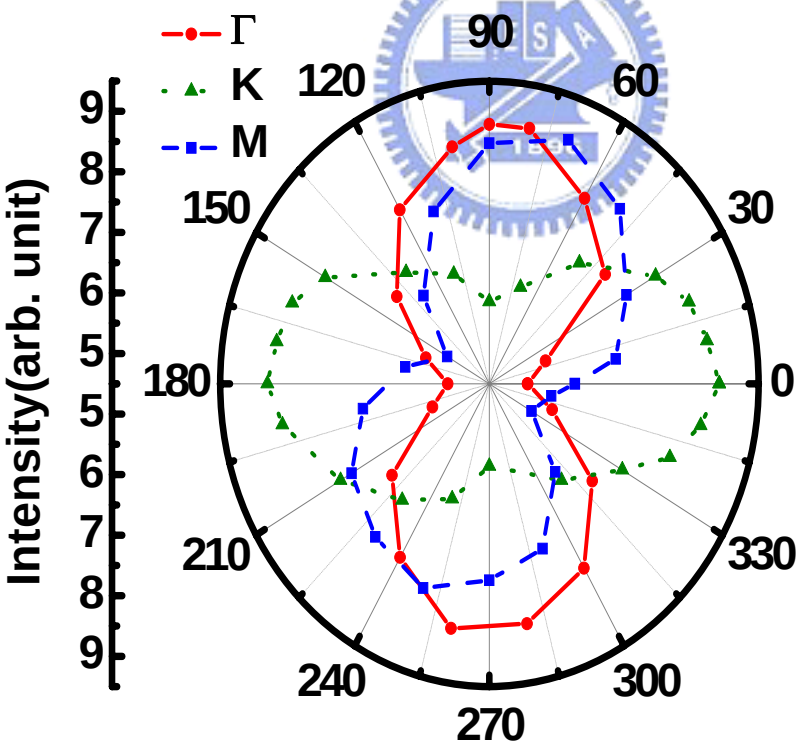

Figure 4.11 The polarization state spectrum for Γ K M band-edge

Divergence angle

We also varied the detecting angle of a fiber which collects light into a spectrometer to measure the laser emission. The fiber is mounted on a stage which could be rotated from -90° to 90°. We measured the emission intensity every 10 degree. Here the 90° is the direction parallel to the sample surface. Fig 4.12 shows the laser emission intensity as a function of the detecting angle of the fiber. The result suggests the laser is vertically emitted. This characteristic is a strong enough evidence to reveal the PCSEL is a kind of considerably excellent single-mode surface emitting laser.

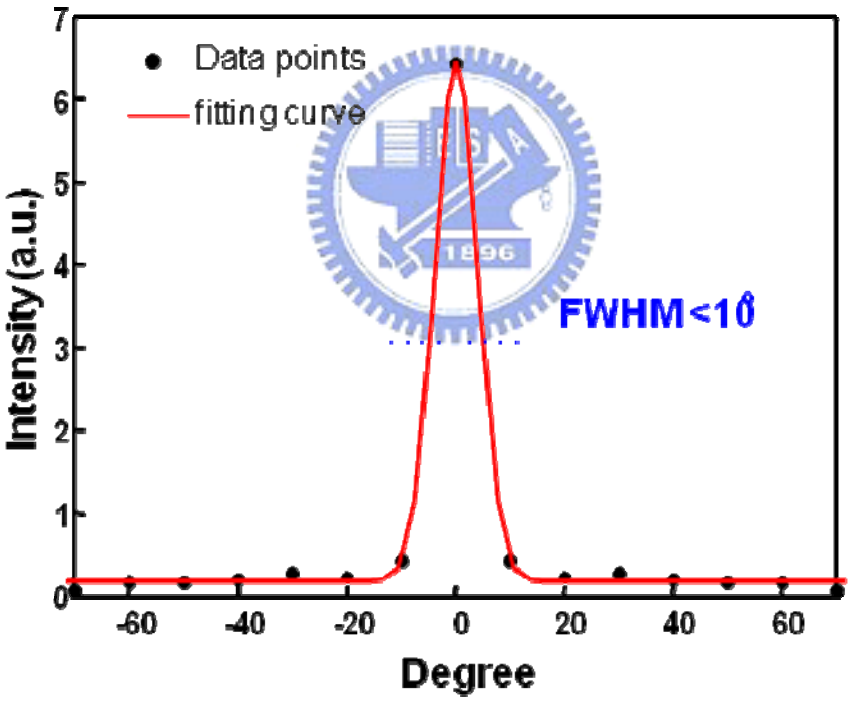

Figure 4.12 The laser intensity of our PCSELs as a function of detecting angle of fiber

Spontaneous emission coefficient

We plot the threshold of our PCSELs device with lattice constant a=234nm with threshold density is about 2.7 mJ/cm2 as shown in Fig 4.13 and further re-plot it in logarithmic scale as shown in Fig. 4.14 and then calculated the difference between the heights of the emission intensities before and after the threshold which should correspond roughly to the value of β. The β value of our PCSEL was estimated about 5×10^{-3}. Interestingly, this value is smaller than the GaN-based vertical cavity surface emitting lasers [3]. However, the β factor is still larger than the typical edge emitting lasers (normally about 10^{-5}) indicating the enhancement of the spontaneous emission into a lasing mode by the high quality factor in GaN-based PCSELs

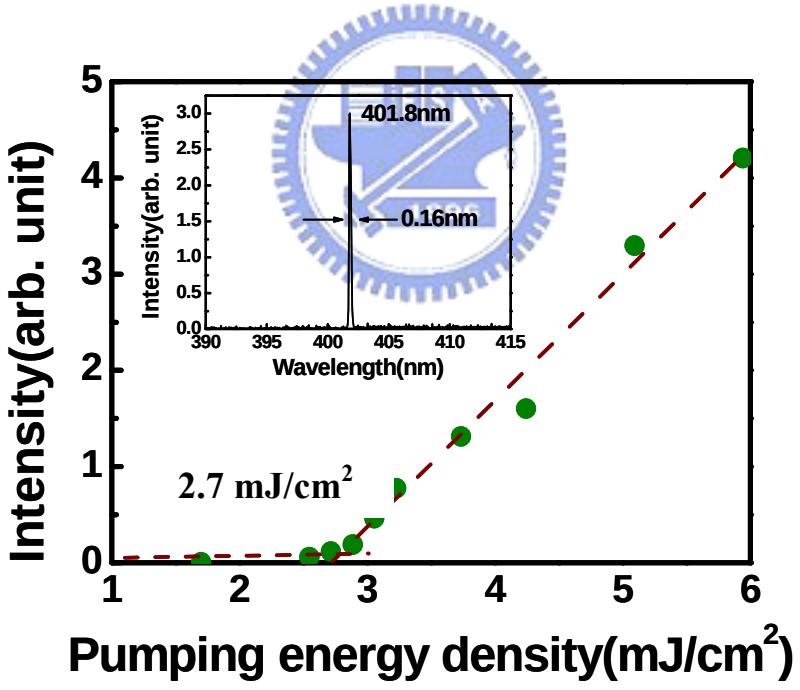

Figure 4.13 Laser emission as a function of pumping energy at room temperature

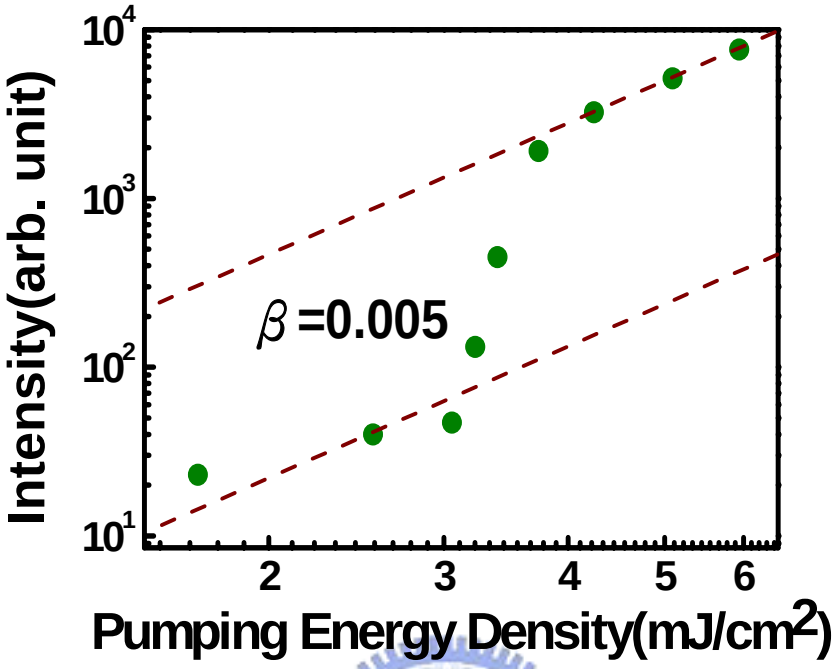

Figure 4.14 Laser emission intensity versus pumping energy in a log scale.

Characteristic temperature

Fig 4.15 shows the semi natural-logarithm plots of the dependence of the threshold pumping energy ($\ln(E_{th})$) on the operation temperature (T_o). The threshold energy gradually increased as the operation rose from 100 to 300K. The relationship between the threshold energy and the operation temperature could be characterized by the equation: $E_{th} = E_o \times e^{T/T_o}$, where T_o is the characteristic temperature and E_o is a constant. Therefore, we obtain a characteristic temperature of about 148K by linear fitting of the experiment data. This value is smaller than VCSEL but similar to EEL. According to theory, T_o is affected by the material and structure. The material for PCSEL is similar to VCSEL which are GaN based material. The structure for VCSEL its cavity length is much shorter than PCSEL results in smaller T_0 property.

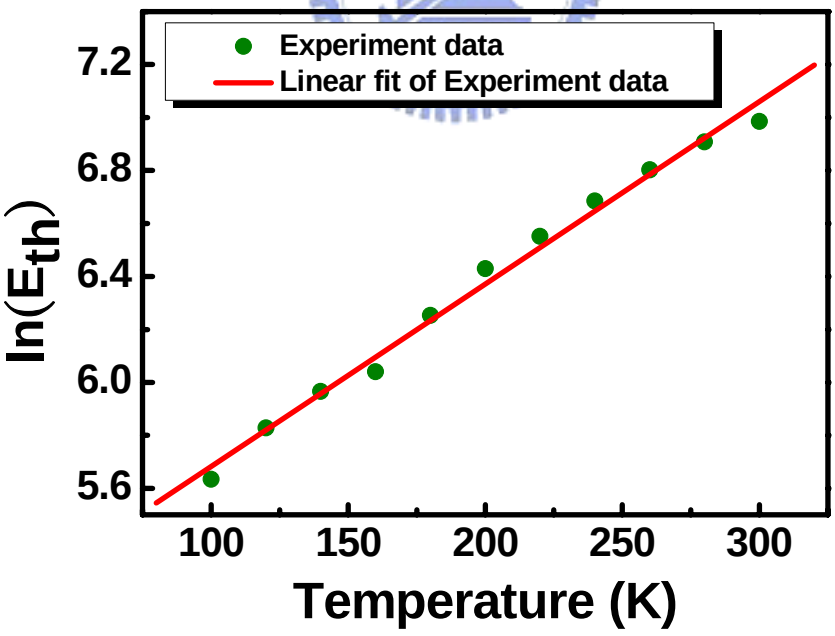

Figure 4.15 The threshold energy as a function of temperature in log scale

4.4 Calculation of coupling coefficient

In section 2.3, the 2D couple-wave model for triangular lattice PC structure has been discussed. Therefore, we further calculate the coupling coefficient at Γ1, K2 M3 band- edge according to the design of our PCSELs.

Γ1 numerical results

The design for lasing action at Γ1 device which parameters are described as follows:

r/a=0.25, a=180nm, nb=2.65, na=1.87, neff=2.495

put these parameters in R-soft software and plot the dispersion diagram for TE-like mode as shown in Fig 4.16

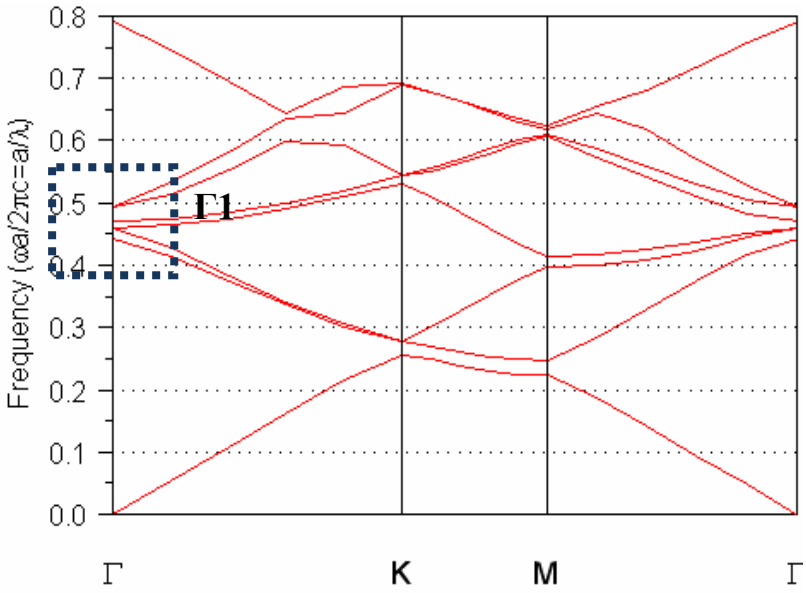

Figure 4.16 Dispersion diagram for TE like mode for Γ1 case

For the band-edge Γ1, there are four cavity mode frequencies, two are degenerated. T The cavity mode frequency can be obtained via simple transform of the normalized frequency which derived from R-soft. The normalized frequency values from lower to higher are 0.4482, 0.4595, 0.4704, and 0.4930. Once the cavity mode frequency at the

individual band-dges can be obtained, we can derive the coupling coefficients κ_1, κ_2, and κ_3 from eqn (2.41) and its values are 17480 cm^{-1},11240 cm^{-1} and 11248 cm^{-1}, respectively. Therefore, for Γ1, the lasing oscillation forms a hexagonal cavity which provided the major significant contribution to support the lasing action.

K2 numerical results

The design for lasing action at K2 device which parameters are described as follows:

r/a=0.26, a=220nm, nb=2.63, na=2.0, neff=2.495

put these parameters in R-soft software and plot the dispersion diagram for TE-like mode as shown in Fig 4.17

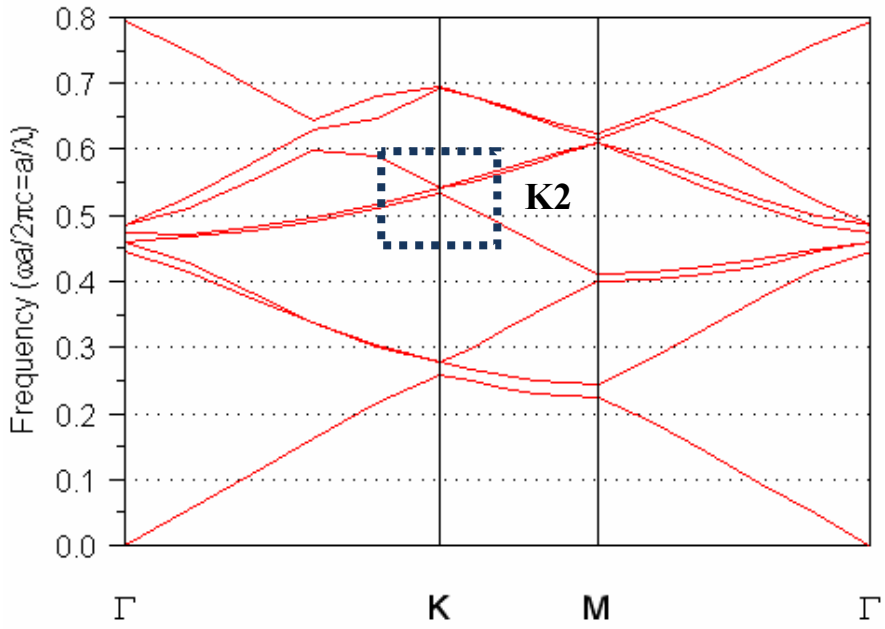

Figure 4.17 Dispersion diagram for TE like mode for K2 case

For the band-edge K2, there are two cavity mode frequencies, one is degenerated. The cavity mode frequency can be obtained via simple transform of the normalized frequency which derived from R-soft. The normalized frequency values from lower to

higher are 0.5326 and 0.5413. Once the cavity mode frequency at the individual band-edges can be obtained, we can derive the coupling coefficients κ from eqn (2.45) is 4089 cm^{-1}. Therefore, for K2, the lasing oscillation forms a triangular cavity which provided energy to support the lasing action

M3 numerical results

The design for lasing action at M3 device which parameters are described as follows:

r/a=0.266, a=247nm, nb=2.64, na=2.01, neff=2.495

put these parameters in R-soft software and plot the dispersion diagram for TE-like mode as shown in Fig 4.18

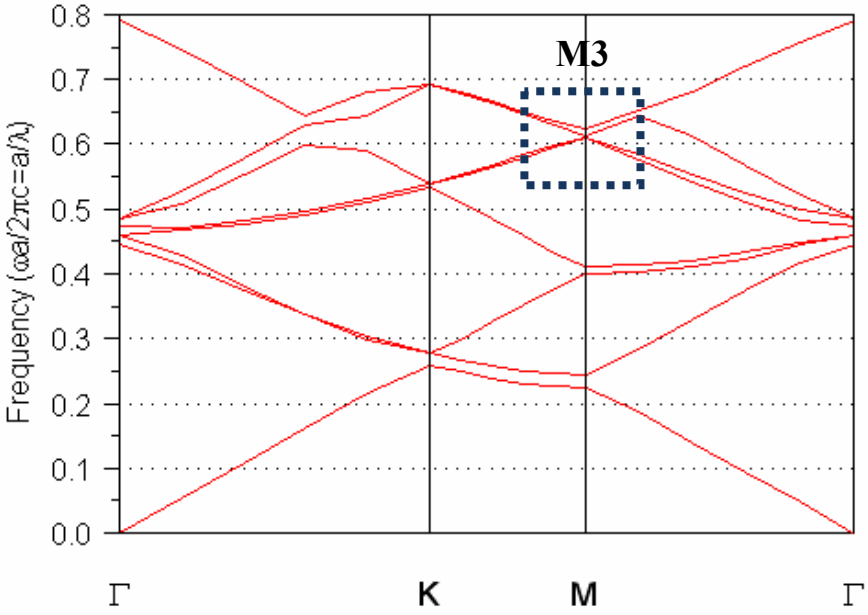

Figure 4.18 Dispersion diagram for TE like mode for M3 case

For the band-edge M3, there are four cavity mode frequencies. The cavity mode frequency can be obtained via simple transform of the normalized frequency which derived from R-soft. The normalized frequency values from lower to higher are

0.60898, 0.60943, 0.61409, and 0.62335. Once the cavity mode frequency at the individual band-edges can be obtained, we can derive the coupling coefficients κ_1, κ_2, and κ_3 from eqn (2.49) and its values are 1241 cm^{-1},1356 cm^{-1} and 2683 cm^{-1}, respectively. Therefore, we know the lasing oscillation back and forth provided the major significant contribution to support the lasing action.

The threshold gain is determined by two factors, one is the gain medium and the other is coupling coefficient. It is expected that the lasing action occurs at Γ1 band edge should have the lowest threshold gain due to the largest coupling coefficient. Therefore, we analyze the threshold gain of PCSELs with its r/a, ranges from 0.25 to 0.26, as a function of normalized frequency as shown in Fig 4.19. It is obvious to see the Γ1 indeed has the lowest threshold gain and M3 has highest threshold gain which correspond with our expectation. In the future, for the electrical pump PCSELs fabrication, one can follow this rule and design for Γ1 group to achieve lasing action.

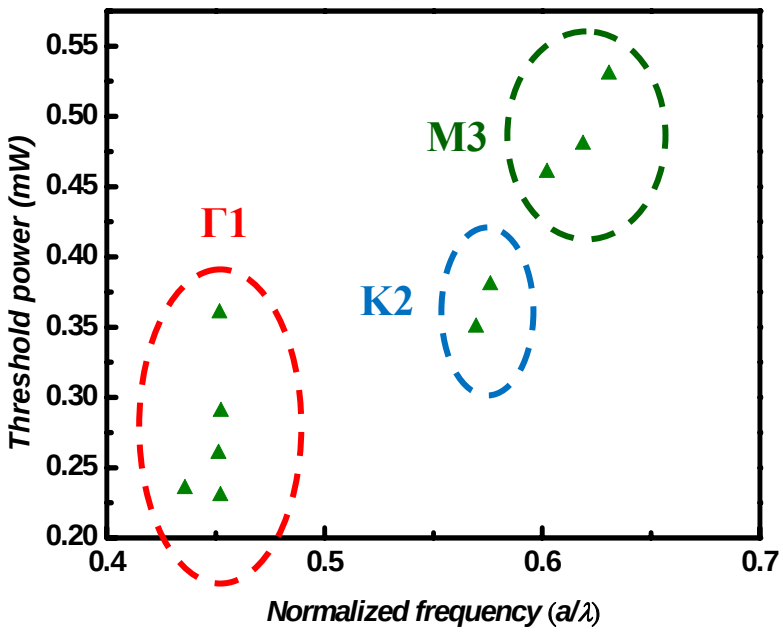

Figure 4.19 The threshold power versus normalized frequency for Γ1 K2 M3 groups

References

1. M. Imada, A. Chutinan, S. Node, and M. Mochizuki, *Phy. Rev. B*, 65, 195306 (2002)

2. S. L. Chuang, Physics of Optoelectronic Devices, *John Wiley & Sons, Inc* (1995)

3. C. C. Kao, T. C. Lu, H. W. Huang, J. T. Chu, Y. C. Peng, H. H. Yao, J. Y. Tsai, T. T. Kao, H. C. Kuo, *IEEE Photon. Tech. Lett*., 18 (2006)

Chapter 5

Conclusion

The GaN-based 2D photonic crystal surface emitting lasers are fabricated and measured in this thesis. The lasing action is achieved under the optical pumping system at the room temperature with a threshold pumping energy density of about 3.5mJ/cm2. Moreover, the laser emits one dominant wavelength of 424.33nm with a linewidth of about 1.1Å. All normalized frequency of investigated PC lasing wavelength can correspond to three band-edge frequencies (Γ1, K2, M3), which indicates the lasing action can only occur at specific band-edges. Polarization states confirm the existence of lasing modes at different band-edge (Γ1, K2, M3). The degree of polarization and divergent angle of the laser emission is about 53% and smaller than 10^{o}, respectively. The characteristic temperature is about 148K. The coupling coefficient at different band-edge (Γ1, K2, M3) can be obtained based on 2D couple-wave model. Furthermore, the threshold gain at Γ1 is the lowest which corresponds to the highest coupling coefficient. All the experiment results indicate that GaN-based PCSELs could be the highly potential optoelectronic device for the next generation lasers.